

Determination of the Cosmic Distance Scale from Sunyaev-Zel'dovich Effect and *Chandra* X-ray Measurements of High Redshift Galaxy Clusters

Massimiliano Bonamente^{1,2}, Marshall K. Joy¹, Samuel J. LaRoque³, John E. Carlstrom^{3,4}, Erik D. Reese⁵ and Kyle S. Dawson⁶

¹*NASA Marshall Space Flight Center, Huntsville, AL*

²*Department of Physics, University of Alabama, Huntsville, AL*

³*Department of Astronomy and Astrophysics, University of Chicago, Chicago, IL
and*

Kavli Institute for Cosmological Physics, University of Chicago, Chicago, IL

⁴*Department of Physics, University of Chicago, Chicago, IL
and*

Enrico Fermi Institute, University of Chicago, Chicago, IL

⁵*Physics Department, University of California, Davis, CA*

⁶*Physics Department, University of California, Berkeley, CA
(now at Lawrence Berkeley National Laboratory)*

ABSTRACT

We determine the distance to 38 clusters of galaxies in the redshift range $0.14 \leq z \leq 0.89$ using X-ray data from *Chandra* and Sunyaev-Zeldovich Effect data from the *Owens Valley Radio Observatory* and the *Berkeley-Illinois-Maryland Association* interferometric arrays. The cluster plasma and dark matter distributions are analyzed using a hydrostatic equilibrium model that accounts for radial variations in density, temperature and abundance, and the statistical and systematic errors of this method are quantified. The analysis is performed via a Markov chain Monte Carlo technique that provides simultaneous estimation of all model parameters. We measure a Hubble constant of $H_0 = 76.9 \pm^{3.9}_{3.4} \pm^{10.0}_{8.0}$ km s⁻¹ Mpc⁻¹ (statistical followed by systematic uncertainty at 68% confidence) for an $\Omega_M = 0.3$, $\Omega_\Lambda = 0.7$ cosmology. We also analyze the data using an isothermal β model that does not invoke the hydrostatic equilibrium assumption, and find $H_0 = 73.7 \pm^{4.6}_{3.8} \pm^{9.5}_{7.6}$ km s⁻¹ Mpc⁻¹; to avoid effects from cool cores in clusters, we repeated this analysis excluding the central 100 kpc from the X-ray data, and find $H_0 = 77.6 \pm^{4.8}_{4.3} \pm^{10.1}_{8.2}$ km s⁻¹ Mpc⁻¹ (statistical followed by systematic uncertainty at 68% confidence). The consistency between the models illustrates the relative insensitivity of SZE/X-ray determinations of H_0 to the details of the

cluster model. Our determination of the Hubble parameter in the distant universe agrees with the recent measurement from the *Hubble Space Telescope* key project that probes the nearby universe.

Subject headings: cosmology: cosmic microwave background; cosmology: distance scale; X-rays: galaxies: clusters

1. Introduction

Combined analysis of radio and X-ray data provides a method to determine directly the distances to galaxy clusters. Galaxy clusters are the largest gravitationally collapsed structures in the universe, with a hot diffuse plasma ($T_e \sim 10^7 - 10^8$ K) that fills the intergalactic space. Cosmic microwave background (CMB) photons passing through this hot intracluster medium (ICM) have a $\sim 1\%$ chance of inverse Compton scattering off the energetic electrons, causing a small (~ 1 mK) distortion of the CMB spectrum, known as the Sunyaev-Zel'dovich Effect (SZE: Sunyaev & Zel'dovich 1970, 1972; for reviews see Birkinshaw 1999; Carlstrom, Holder, & Reese 2002). The same hot gas emits X-rays primarily through thermal bremsstrahlung. The SZE is a function of the integrated pressure, $\Delta T \propto \int n_e T_e d\ell$, where n_e and T_e are the electron number density and temperature of the hot gas, and the integration is along the line-of-sight. The X-ray emission scales as $S_X \propto \int n_e^2 \Lambda_{ee} d\ell$, where Λ_{ee} is the X-ray cooling function. The different dependences on density, along with a model of the cluster gas, enable a direct distance determination to the galaxy cluster. This method is independent of the extragalactic distance ladder and provides distances to high redshift galaxy clusters.

The ~ 1 mK SZE signal proved challenging for initial searches, but recent improvements in both technology and observational strategies have made observations of the SZE fairly routine. High signal-to-noise ratio (S/N) detections of the SZE have been made with single dish observations at radio wavelengths (Birkinshaw and Hughes 1994; Herbig et al. 1995; Myers et al. 1997; Hughes and Birkinshaw 1998; Mason et al. 2001), millimeter wavelengths (Holzapfel et al. 1997a,b; Pointecouteau et al. 1999, 2001) and submillimeter wavelengths (Lamarre et al. 1998; Komatsu et al. 1999), while interferometric observations at centimeter wavelengths have produced images of the SZE (Jones et al. 1993; Grainge et al. 1993; Carlstrom et al. 1996, 2000; Grainge et al. 2002; Reese et al. 2000, 2002; Grego et al. 2000, 2001; La Roque et al. 2003; Udomprasert et al. 2004).

SZE/X-ray distances provide a measure of the Hubble constant that is independent of the extragalactic distance ladder and probe high redshifts, well into the Hubble flow. The

SZE/X-ray determinations of H_0 bridge the gap between observations of nearby objects (e.g. the Hubble Space Telescope Key Project, Freedman et al. 2001) and expansion values inferred from CMB anisotropy (Spergel et al. 2003) and supernova (Riess et al. 2005) measurements. Previous SZE/X-ray determinations of the Hubble parameter have progressed from analysis of individual galaxy clusters, to samples of a few (Myers et al. 1997; Mason et al. 2001; Jones et al. 2005), up to a sample of 18 galaxy clusters using ROSAT X-ray data (Reese et al. 2002; for reviews see Reese 2004 and Carlstrom, Holder, & Reese 2002). In most cases, simple isothermal β models were adopted for the cluster gas, since the data did not warrant a more sophisticated treatment.

We present a Markov chain Monte Carlo joint analysis of interferometric SZE observations and *Chandra* X-ray imaging spectroscopy observations of a sample of 38 galaxy clusters with redshifts $0.14 \leq z \leq 0.89$. The unprecedented spatial resolution of *Chandra* combined with its simultaneous spectral resolution allow more realistic modeling of the intracluster plasma than previous studies, thus enabling a more accurate determination of the Hubble constant.

2. Observations of galaxy clusters

2.1. Interferometric Sunyaev-Zel'dovich effect data

Interferometric radio observations of the 38 clusters in Table 1 were performed at the Berkeley-Illinois-Maryland Association observatory (*BIMA*) and at the Owens Valley Radio Observatory (*OVRO*). The arrays were equipped with 26-36 GHz receivers to obtain maps of the Sunyaev-Zel'dovich Effect (SZE) toward the clusters (Carlstrom et al. 1996, 2000; Reese et al. 2000). These frequencies are on the Rayleigh-Jeans end of the microwave spectrum, and the scattering with cluster electrons causes an intensity decrease that, in terms of brightness temperature, corresponds to a change in T_{CMB} of order -1 mK.

Most of the *OVRO* and *BIMA* telescopes were placed in a compact configuration to maximize the sensitivity on angular scales subtended by distant clusters (typically $\sim 1'$) and a few telescopes were placed at longer baselines for simultaneous point source imaging (Reese et al. 2002). The SZE data consist of the position in the Fourier domain (u - v plane) and the visibilities — the real and imaginary Fourier component pairs as functions of u and v , which are the Fourier conjugate variables to right ascension and declination. The effective resolution of the interferometer, the synthesized beam, depends on the u - v coverage and is therefore a function of the array configuration and source position. A typical size for the synthesized beam of our observations is $\sim 1'$, as shown in Figure 1. The SZE data were

reduced using the MIRIAD (Sault et al. 1995) and MMA (Scoville et al. 1993) software packages and images were made with DIFMAP (Pearson et al. 1994) software. Absolute flux calibration was performed using Mars observations adopting the brightness temperature from the Rudy (1987) Mars model. The gain was monitored with observations of phase calibrators, and remained stable at the 1% level over a period of months. Data were excised when one telescope was shadowed by another, when cluster observations were not bracketed by two phase calibrators, when there were anomalous changes in the instrumental response between calibrator observations, or when there was spurious correlation. Positions of point sources were identified using the long baseline data; their fluxes are included as free parameters in the model, using the same methodology as Reese et al. (2002). Additional details of the SZE data analysis are provided in Reese et al. (2002) and Grego et al. (2000).

2.2. *Chandra* X-ray data

The *Chandra* X-ray data for the 38 clusters in our sample were obtained primarily through the Guaranteed Time program of Leon van Speybroeck. The observations were performed with the ACIS-I and ACIS-S detectors. The two ACIS instruments provide spatially resolved X-ray spectroscopy and imaging with an angular resolution of $\sim 0.5''$ and with energy resolution of $\sim 100-200$ eV. Data analysis was performed with the CIAO software (version 3.2) and the CALDB calibration information (version 3.1) provided by the *Chandra* calibration team (*Chandra* Interactive Analysis of Observations, <http://cxc.harvard.edu/ciao/>).

The first step in the data analysis was to process the Level 1 data to correct for the charge transfer inefficiency of the ACIS detectors. We then generated a Level 2 event file applying standard filtering techniques: we selected grade=0,2,3,4,6, status=0 events (as defined in the Chandra Proposers Observatory Guide) and filtered the event file for periods of poor aspect solution using the good time interval (GTI) data provided with the observations. Periods of high background count rates were occasionally present, typically due to Solar flares (Markevitch 2001). We discarded these periods using an iterative procedure in which we constructed a light-curve of a background region in 500 second bins, and time intervals that were in excess of the median count rate by more than 3σ were discarded from the dataset. The Chandra instruments are affected by the buildup of a contaminant on the optical blocking filter located along the optical path to the ACIS detector; we accounted for this efficiency reduction using CIAO and CALDB. Spectra were accumulated in concentric annuli centered at the peak of the X-ray emission, each containing approximately the same number of source photons after removal of point sources. Both images and spectra were limited to 0.7-7 keV in order to exclude the low-energy and high-energy data that are more

strongly affected by background and by calibration uncertainties. The X-ray images were binned in $1.97''$ pixels; this sets the limiting angular resolution of our X-ray data, as the *Chandra*/ point response function in the center of the X-ray image is smaller than our adopted pixel size. The X-ray background was measured for each cluster exposure, using peripheral regions of the detector (ACIS-S) or adjacent detector chips (ACIS-I) that are source free. Additional details of the *Chandra* X-ray data analysis are provided in Section 2 of Bonamente et al. (2004).

Images of the X-ray surface brightness of selected clusters are shown in Figure 1, with SZE contours overlaid, and in Appendix 1 for all 38 clusters. *Chandra* also provides spatially-resolved spectroscopy that allows a determination of the temperature and metal abundance of the hot plasma. The spectral properties of the plasma are obtained by fits to an optically thin emission model, with absorbing column N_H fixed at the Galactic value. The uncertainty in N_H of $\sim 10^{19}$ cm $^{-2}$ (Dickey and Lockman 1990) results in uncertainties in the measured temperatures of less than 1%, and therefore has a negligible effect in the measurement of the cluster distances. In Figure 1 we show the radial profiles of the X-ray surface brightness and of the plasma temperature for several representative clusters, along with their best fit curves as determined from the modeling described in the next Section; radial brightness and temperature profiles for the full cluster sample are presented in Appendix 2 and 3.

In Figure 2 we show the composite radial temperature profiles for the 38 clusters. The clusters containing plasma with a central cooling time $t_{cool} \leq 0.5t_{Hubble}$, which we refer to as the “cool core” sample, are shown on top, while clusters with longer cooling times are shown on the bottom¹. The temperature profiles for the 38 clusters lie within the envelope of the 21 clusters observed by BeppoSAX (see Fig. 3, Fig. 4 and Table 2 of De Grandi and Molendi 2002). The spectra were extracted in concentric annuli that contain a similar number of photons in each annulus for each cluster. The radial temperature profile data for all clusters, including the temperature, the background-subtracted counts and the χ^2 , are reported in Appendix 3 (Table 7). Metal abundances of the hot cluster plasma have a marginal effect on the X-ray cooling function (see Section 3). We assume the De Grandi et al. (2004) abundance profile in our analysis, which is consistent with our measured abundances.

¹The clusters with $t_{cool} \leq 0.5t_{Hubble}$ are Abell 586, MACS J0744.8+3927, ZW 3146, Abell 1413, MACS J1311.0-0310, Abell 1689, RX J1347.5-1145, MS 1358.4+6245, Abell 1835, MACS J1423.8+2404, RX J2129.7+0005, Abell 2163, Abell 2204 and Abell 2261. The Hubble time is approximately $t_{Hubble} \simeq H_0^{-1}$ (Carroll, Press and Turner 1992) with $H_0 = 72$ km s $^{-1}$ Mpc $^{-1}$ and the cooling time ($t_{cool} \simeq 3k_B T / 2\Lambda_{ee} n_e$) is calculated using the central density and the temperature from an isothermal β model fit.

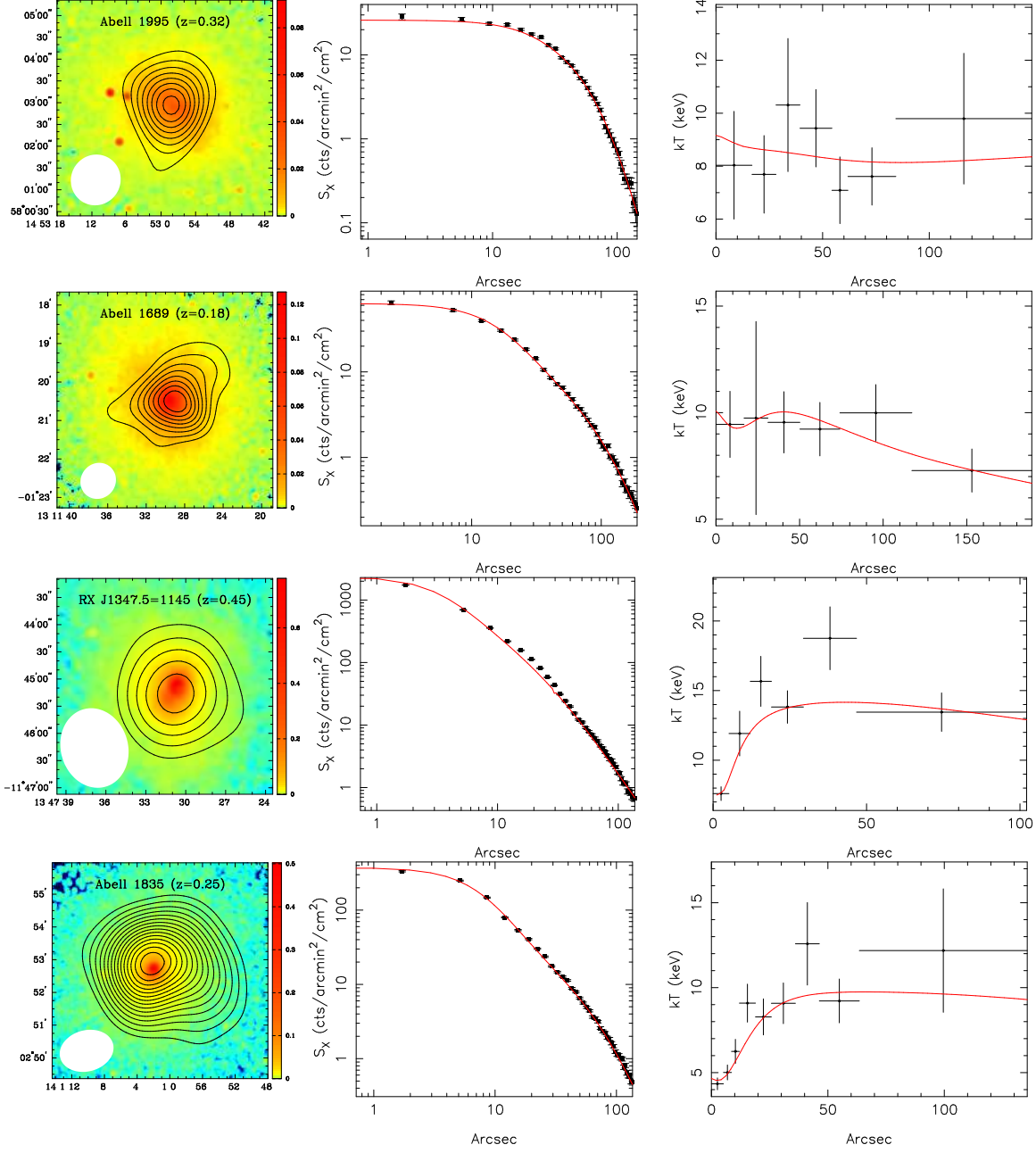


Fig. 1.— (Left) *Chandra* images of the X-ray surface brightness in 0.7-7 keV band in units of counts pixel⁻¹ (1.97'' pixels) for selected clusters. Overlaid are the SZE decrement contours, with contour levels (+1,-1,-2,-3,-4,...) times the rms noise in each image; the full-width-at-half-maximum of the SZE synthesized beam (effective point-spread function) is shown in the lower left corner. The X-ray images were smoothed with a $\sigma = 2''$ Gaussian kernel. (Center) Radial profile of the background subtracted X-ray surface brightness; the solid line is the best-fit model obtained with the parameters of Table 2. (Right) Radial profiles of the *Chandra* temperatures, the solid line is the best-fit hydrostatic equilibrium model with the parameters of Table 2.

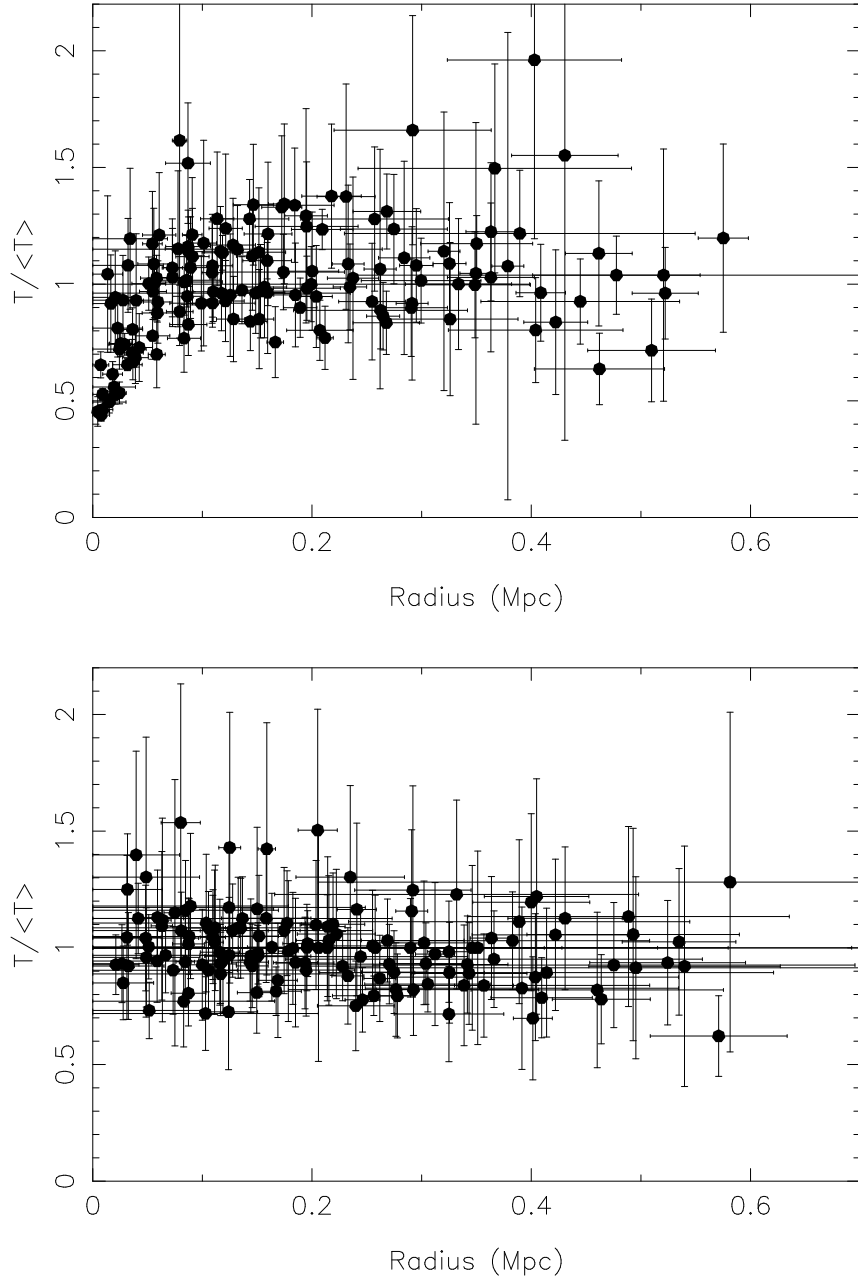


Fig. 2.— Temperature profiles for clusters with central cooling time $t_{cool} \leq 0.5 \times t_{Hubble}$ (top) and for clusters with $t_{cool} > 0.5 \times t_{Hubble}$ (bottom). We assume the best-fit Hubble constant of Section 4.1 and $\Omega_M = 0.3$, $\Omega_\Lambda = 0.7$. $T/\langle T \rangle$ is plotted as function of projected radius.

3. Measuring distances with X-ray and Sunyaev-Zel'dovich Effect data

3.1. The hydrostatic equilibrium model

To determine the distance to a cluster, we must first construct a realistic model for the cluster gas distribution. At the center of clusters the density may be high enough that the radiative cooling time-scale is less than the cluster's age, leading to a reduction in temperature and an increase in central density. This increases the central X-ray emissivity in the *Chandra* passband, as shown in Figure 1 for the clusters *RXJ 1347.5-1145* and Abell 1835. At large radii, the density of the gas is sufficiently low that X-ray emission can be sustained for cosmological periods without significant cooling. Cool core clusters effectively exhibit two components: a centrally concentrated gas peak and a broad, shallower distribution of the gas. This phenomenon motivates the modelling of the gas density with a function of the form:

$$n_e(r) = n_{e0} \cdot \left[f \left(1 + \frac{r^2}{r_{c1}^2} \right)^{-\frac{3\beta}{2}} + (1 - f) \left(1 + \frac{r^2}{r_{c2}^2} \right)^{-\frac{3\beta}{2}} \right] \quad (1)$$

This shape generalizes the single β -model profile, introduced by Cavaliere and Fusco-Femiano (1976) and commonly used to fit X-ray surface brightness profiles, to a double β -model of the density that has the freedom of following both the central spike in density and the more gentle outer distribution. A double β -model of the surface brightness was first used by Mohr et al. (1999) to fit X-ray data of galaxy clusters; the density model of Equation 1 was further developed by La Roque (2005). The quantity n_{e0} is the central density, f governs the fractional contributions of the narrow and broad components ($0 \leq f \leq 1$), r_{c1} and r_{c2} are the two core radii that describe the shape of the inner and outer portions of the density distribution and β determines the slope at large radii (the same β is used for both the central and outer distribution in order to reduce the total number of degrees of freedom).

The X-ray surface brightness is related to the gas density as

$$S_X = \frac{1}{4\pi(1+z)^4} \int n_e^2 \Lambda_{ee} dl \quad (2)$$

where z is the cluster redshift, n_e is the electron density of the plasma (Equation 1), Λ_{ee} is the X-ray cooling function, and the integration is performed along the line of sight l . We calculate Λ_{ee} as a function of plasma temperature and energy in the rest frame of the cluster, including contributions from relativistic electron-ion thermal bremsstrahlung, electron-electron thermal bremsstrahlung, recombination, and two photon processes; the cooling function is then redshifted to the detector frame, convolved with the telescope and detector response, and integrated over the 0.7-7 keV *Chandra* bandpass, following the method described in Reese et

al. (2000). The calculation of Λ_{ee} requires a temperature profile in order to perform the integration, which we determine from our Chandra data (Figure 2). The appropriate response for each image was generated from CIAO.

The SZE decrement is proportional to the integrated gas pressure as

$$\Delta T_{CMB} = f_{(x,T_e)} T_{CMB} \int \sigma_T n_e \frac{k_B T_e}{m_e c^2} dl \quad (3)$$

where $f_{(x,T_e)}$ is the frequency dependence of the SZE, $x = h\nu/k_B T_{CMB}$ and $f_{(x,T_e)} \simeq -2$ at our observing frequency of 30 GHz, $T_{CMB} = 2.728$ K (Fixsen et al. 1996), σ_T is the Thomson cross section, k_B is the Boltzmann constant, c is the speed of light in vacuum, m_e is the electron mass, T_e the electron temperature, and the integration is along the line of sight.

Historically, the cluster distance has been solved for directly by taking advantage of the different density dependences of the X-ray emission and SZE decrement (e.g., Hughes, Birkinshaw and Arnaud 1991; Reese et al. 2002; Bonamente et al. 2004):

$$\begin{aligned} S_X &\propto \int n_e^2 \Lambda_{ee} dl = \int n_e^2 \Lambda_{ee} D_A d\theta \\ \Delta T_{CMB} &\propto \int n_e T_e dl = \int n_e T_e D_A d\theta \end{aligned} \quad (4)$$

The details of the plasma modelling, such as the numerical integration of the density profile, are included in the proportionality constants of Equations 4. The cluster angular diameter distance $D_A \equiv dl/d\theta$, where θ is the line-of-sight angular size, can be inferred with a joint analysis of SZE and X-ray data by assuming a cluster geometry to relate the measured angular size in the plane of the sky to that along the line of sight. For our adopted spherical geometry, these two sizes are equal.

Our model includes the distribution of dark matter in clusters. The baryonic matter reaches hydrostatic equilibrium in the potential well defined by the baryonic and dark matter components, on a time scale that is shorter than the cluster's age (Sarazin 1988). Under spherical symmetry, this results in the condition

$$\frac{dP}{dr} = -\rho_g \frac{d\phi}{dr} \quad (5)$$

where P is the gas pressure, ρ_g is the gas density and $\phi = -GM(r)/r$ is the gravitational potential due to both dark matter and the plasma. Using the ideal gas equation of state for the diffuse cluster plasma, $P = \rho_g k_B T / \mu m_p$ where μ is the mean molecular weight and m_p is the proton mass, one obtains a relationship between the cluster temperature and the cluster

mass distribution:

$$\frac{dT}{dr} = - \left[\frac{\mu m_p}{k_B} \frac{d\phi}{dr} + \frac{T}{\rho_g} \frac{d\rho_g}{dr} \right] = - \left[\frac{\mu m_p}{k_B} \frac{GM}{r^2} + \frac{T}{\rho_g} \frac{d\rho_g}{dr} \right] \quad (6)$$

We combine these hydrostatic equilibrium equations with a dark matter density distribution from Navarro, Frenk and White (1997):

$$\rho_{DM}(r) = \mathcal{N} \left[\frac{1}{(r/r_s)(1+r/r_s)^2} \right] \quad (7)$$

where \mathcal{N} is a density normalization constant and r_s is a scale radius. These model equations are combined with the X-ray and SZE data using a Markov chain Monte Carlo method, described in the following Section.

In Figure 1 the best-fit line (in red) of the X-ray surface brightness is obtained using the density distribution of Equation 1 and the hydrostatic equilibrium model described in this Section. For clusters in which a single β model is an acceptable fit to the X-ray surface brightness ($\chi_r^2 < 1.5$; see Appendix 2), we simplify the density model of Equation 1 by fixing the parameter $f = 0$. We fit spherically symmetric models to all of the clusters, including those which do not appear circular in X-ray and radio observations, as this approach gives an unbiased estimator of cluster distances when a large sample of clusters is used (Sulkanen 1999).

3.2. Parameter estimation using the Markov chain Monte Carlo method

Our model consists of five parameters that describe the gas density (n_{e0} , f , r_{c1} , r_{c2} and β ; Equation 1), two parameters that describe the dark matter density (\mathcal{N} and r_s from Equation 7) and the angular diameter distance D_A . Additional parameters such as the cluster position, point source positions, and point source fluxes are also included. A detailed discussion of radio point sources is provided in Reese et al. (2002). By linking the central densities between the X-ray and SZE datasets, and allowing D_A to vary, the model can be integrated along the line of sight and compared with the X-ray and SZE data simultaneously, according to Equations 2 and 3. The model parameters can also be used with Equation 6 to solve for the cluster temperature profile, which is integrated along the line of sight and compared with the spectral data as described below. The Markov chain Monte Carlo (MCMC) method used to estimate the model parameters is described in Bonamente et al. (2004). In this Section we provide a brief overview of the method, focusing on the changes we applied to accommodate the new hydrostatic equilibrium model of Section 3.1.

The first step of the Markov chain Monte Carlo method is the calculation of the joint likelihood \mathcal{L} of the X-ray and SZE data with the model. This calculation follows three independent steps, one for each of the datasets involved: SZE data, X-ray images, and X-ray spectra. The likelihood calculation for the SZE data is performed directly in the Fourier plane, where the data are taken and where we understand the noise properties of the data. The likelihood is given by

$$\ln(\mathcal{L}_{SZE}) = \sum_i \left(-\frac{1}{2} (\Delta R_i^2 + \Delta I_i^2) \right) W_i \quad (8)$$

where ΔR_i and ΔI_i are the difference between model and data for the real and imaginary components at each point i in the Fourier plane, and W_i is a measure of the Gaussian noise ($1/\sigma^2$).

Since the X-ray counts are distributed according to Poisson statistics, the likelihood is given by

$$\ln(\mathcal{L}_{image}) = \sum_i [D_i \ln(M_i) - M_i - \ln(D_i!)] \quad (9)$$

where M_i is model prediction (including cluster and background components), and D_i is the number of counts detected in pixel i . For details on the X-ray/SZE joint analysis, see Reese et al. (2000).

The spectral likelihood is calculated by comparing the predicted temperature profile with the observed one:

$$\ln(\mathcal{L}_{spectra}) = -\frac{1}{2} \chi^2 - \frac{1}{2} \sum_i \ln(2\pi\sigma_i^2) \quad (10)$$

where i labels the bins in the temperature profile (Figure 2), $\chi^2 \equiv \sum_i ([T_i - M_i]/\sigma_i)^2$, T_i and M_i are the measured and model-predicted temperatures, and σ_i is the measured temperature uncertainty. The last term on the right in Equation 10 depends only on the data and will cancel when performing the likelihood ratio test. Likelihood evaluation for the spectral data requires another numerical integration to solve for $T_e(r)$, according to Equation 6. This temperature profile is weighted by the square of the density and the cooling function (Equation 2) and then integrated along the line of sight to determine the emission-weighted temperature profiles, which can be directly compared with the measured temperature profile. The joint likelihood of the spatial and spectral models is given by

$$\mathcal{L} = \mathcal{L}_{SZE} \cdot \mathcal{L}_{image} \cdot \mathcal{L}_{spectra}.$$

A Markov chain is a sequence of model parameters constructed with the property that the model parameters appear in the chain with a frequency that is proportional to their

posterior probability, i.e., the probability of occurrence in the light of the current observations. We start by assuming vague *prior* probability distributions for all parameters as top-hat functions between two extreme values. The first link of the MCMC is chosen as the midpoint of the prior distributions. We then select a candidate for the next link in the chain using a *proposal* distribution, in our case a simple top-hat function of constant width around the previous parameter values. These candidate parameter values are accepted into the chain or rejected according to the Metropolis-Hastings criterion (Metropolis 1953, Hastings 1970) that takes into account the likelihood information. This process is iterated for a large number of steps, which we chose as 100,000. This number ensures that the MCMC has reached convergence towards the posterior probability distribution functions of the parameters (Bonamente et al. 2004). Convergence is tested using the Raftery-Lewis test (Raftery and Lewis 1992; Gilks et al. 1996), the Gelman-Rubin test (Gelman and Rubin 1992) and the Geweke test (Geweke 1992). Confidence intervals for the model parameters are obtained by computing the cumulative distribution of the occurrence for each model parameter. We consider the median of the distribution as the best-fit value and calculate 68% confidence intervals around the median.

The results of the MCMC analysis are shown in Table 2, in which we report the best-fit values of \mathcal{N} , r_s , n_{e0} , r_{c1} , β , f , r_{c2} and D_A for each cluster.

3.3. Uncertainty analysis

The uncertainties in Table 2 represent the photon-counting statistical uncertainties of the X-ray images and spectra, and the statistical uncertainty of the SZE observations, as described in Section 3.2. Other sources of statistical and systematic uncertainty that affect our measurements are discussed in this Section and listed in Table 3. For comparison with the uncertainties encountered in previous studies, see Reese et al. (2002). We note that the Chandra and OVRO/BIMA sample allows us to obtain a distance scale measurement averaged over a large number of clusters; this ensemble average significantly reduces the impact of the single-cluster statistical uncertainties shown in Tables 2 and 3.

In the uncertainty analysis we make use of the following relationship that follows from Equation 4, as shown in Bonamente et al. (2004):

$$D_A \propto \frac{\Delta T_{CMB}^2 \Lambda_{ee}}{S_X T_e^2} \quad (11)$$

Note that D_A is proportional to ΔT_{CMB}^2 and $T_e^{3/2}$ (since $\Lambda_{ee} \propto T_e^{1/2}$), so the distance determination is strongly dependent on the accuracy of the SZE decrement and X-ray temperature

measurements.

3.3.1. Uncertainty in Galactic N_H

In the spectral fits of Section 2.2 we used the HI column densities of Dickey and Lockman (1990), which have an uncertainty of $\sigma_{N_H} = 1 \times 10^{19} \text{ cm}^{-2}$. A variation of the HI column density will primarily affect the best-fit X-ray temperature. The temperature, in turn, affects the measurement of cluster distances through Equation 11, $D_A \propto \Lambda_e T_e^{-2}$, in which the X-ray cooling function is $\Lambda_{ee} \propto T^{0.5}$. We obtained spectral fits of our clusters using $N_H + \sigma_{N_H}$ and $N_H - \sigma_{N_H}$ as the HI column densities, and found that the best-fit temperatures change by less than 0.5%. The uncertainty in Galactic N_H therefore results in a D_A uncertainty of $\leq 1\%$ ($D_A \propto T_e^{-1.5}$).

3.3.2. Cluster asphericity

Most clusters do not appear circular in X-ray or radio observations (e.g., Mohr et al. 1995). Numerical simulations by Sulkanen (1999) show that a spherical model fit to triaxial X-ray and SZE clusters yields an unbiased estimate of cluster distance when a large ensemble of clusters is used; the standard deviation of the measured distance for one cluster is $\sim 15\%$.

3.3.3. Small scale clumps in the intracluster gas

Clumping of the intracluster medium on scales smaller than the Chandra resolution is a potential source of systematic error. The presence of clumps enhances the measured X-ray emission (S_X) by the factor:

$$C \equiv \frac{\langle n_e^2 \rangle}{\langle n_e \rangle^2} \geq 1. \quad (12)$$

A factor $C > 1$ results in a measured angular diameter distance ($D_A \propto S_X^{-1}$) that is lower than what one measures if no clumping is present, and such D_A should be increased by a factor of C if clumping occurs. In this case, the resulting best-fit H_0 would decrease.

Concurrent studies by LaRoque et al. (2006) suggest that as long as the clumps of X-ray emission observed by *Chandra* are excised from the data, the clusters in this sample are not affected by additional clumping of the hot gas. We therefore do not include this source of uncertainty in our error analysis. There is indication that clumpiness of the gas may be a

factor for high-redshift clusters (Jeltema et al. 2005), and this effect may in principle lead to increased scatter at large z in Figure 3.

3.3.4. Point sources in the field

Undetected radio point sources near the cluster center mask the central decrement. According to Equation 11, $D_A \propto \Delta T_{CMB}^2$, and an underestimate of the SZE decrement will result in an underestimate of the cluster distance. The synthesized beam of the SZE instrument also has negative sidelobes, and therefore overestimates of the decrement are also possible. A detailed treatment of the effect of point sources by La Roque et al. (2006) using this cluster sample result in a $\sim 8\%$ uncertainty in the determination of D_A .

For the X-ray data, the superior angular resolution of Chandra allows one to locate the point sources and mask them from the analysis, so no uncertainty from undetected X-ray point sources is introduced.

3.3.5. Kinetic SZE effect and CMB anisotropies

Peculiar velocities of clusters introduce a distortion in the CMB spectrum, known as the kinetic SZE. For a typical line-of-sight peculiar velocity of 300 km s^{-1} (Watkins 1997, Colberg et al. 2000) and a cluster of $T_e = 8 \text{ keV}$, the kinetic SZE is 4% of the thermal SZE. Since $D_A \propto \Delta T_{CMB}^2$, the kinetic SZE effect introduces an uncertainty of 8% to the determination of cluster distances.

Limits on CMB anisotropies have been measured by Dawson et al. (2001, 2006) and Holzapfel et al. (2000) with BIMA at the frequency and angular scales of the observations presented in this paper. The 68% confidence upper limit is $\Delta T_{CMB} < 19 \mu\text{K}$ at $l \sim 5500$ ($\sim 2'$ scales). This results in a 68% uncertainty of $\leq 1\%$ in the measurement of ΔT_{CMB} , and $\leq 2\%$ in the measurement of D_A . Both of these effects are expected to average out for a sample of clusters widely separated on the sky.

3.3.6. Radio halos and relics

Extended steep-spectrum nonthermal radio halo sources have been detected in the center of several clusters (Giovannini and Feretti 2000; Giovannini et al. 1999; Hanish 1982), and similar extended sources (radio relics) have also been found in other clusters at large radii

from the cluster core (Giovannini and Feretti 2004; Feretti 2004). The on-center radio halo sources can mask the SZE decrement, resulting in an underestimate of D_A . Reese et al. (2002) determined that the average effect of a radio halo at the BIMA and OVRO frequency is small: $\sim 1.5\%$ of the thermal decrement. We include a one-sided $+3\%$ systematic uncertainty in the D_A measurement to account for the possible presence of extended non-thermal radio halo emission in the cluster core. The frequency of occurrence and the flux of radio relic and radio halo sources are similar (Feretti 2004), but radio relics are attenuated by the interferometer due to their large displacement from the cluster center; we estimate that the systematic uncertainty due to radio relic sources is negligible ($< 1\%$).

3.3.7. X-ray background

The X-ray background is measured following the method described in Section 2.2 and in Bonamente et al. (2004). For each cluster, we measure the 0.7-7 keV counts in a background region, with a statistical error equal to the square root of the number of counts, and extract a background spectrum from the same region. We assessed the effect of the X-ray background subtraction on the distance measurements by performing the following analysis. For the spatial analysis, we used the upper and lower limits of the measured background level; in the spectral analysis, we used the temperatures obtained by subtracting the background spectrum, rescaled by an amount equal to \pm the fractional error of the measured background level. These additional MCMC runs resulted in D_A measurements that are within $\sim 2\%$ of those obtained with the nominal background. We therefore add a $\pm 2\%$ uncertainty in the measurement of D_A .

3.3.8. X-ray calibration

The absolute calibration of the Chandra ACIS effective area is known to $\sim 5\%$ in the 0.7-7 keV band of interest (<http://asc.harvard.edu/cal>). This uncertainty affects the D_A measurements directly through the surface brightness terms in Equation 11, resulting in a 5% systematic uncertainty on S_X .

Temperature measurements with Chandra may be subject to systematic offsets caused by effective area and energy calibration errors, which we estimate at 5% (<http://asc.harvard.edu/cal>). According to Equation 11, $D_A \propto \frac{\Lambda_{ee}}{S_X T_e^2}$, where $\Lambda_{ee} \propto T_e^{0.5}$, therefore the effect of the temperature measurement uncertainty results in a $\sim 7.5\%$ uncertainty on the distance for one cluster.

3.3.9. SZE calibration

The absolute calibration of the interferometric observations is known to about 4%, resulting in an uncertainty of 8% in the distance measurement of one cluster. Reese et al. (2002) also studied the effect of imprecisions in the measurement of the BIMA and OVRO primary beams, and conclude that the effect on distance measurements is negligible.

4. Measurement of the Hubble constant

We now use the 38 cluster distances to estimate the Hubble constant. The angular diameter distance D_A is a function of the cluster redshift z , the mass density Ω_M , the dark energy density Ω_Λ , and the Hubble constant H_0 , which is the overall normalization:

$$D_A(z) = \frac{1}{H_0} \cdot \frac{c}{|\Omega_k|^{1/2}(1+z)} \cdot \text{sinn} \left[|\Omega_k|^{1/2} \int_0^z [(1+\zeta)^2(1+\Omega_M\zeta) - \zeta(2+\zeta)\Omega_\Lambda]^{-1/2} d\zeta \right] \quad (13)$$

where the function $\text{sinn}(x)$ is defined as $\sinh(x)$ for $\Omega_k > 0$, $\text{sinn}(x) = x$ for $\Omega_k = 0$, $\text{sinn}(x) = \sin(x)$ for $\Omega_k < 0$, and $\Omega_k = 1 - \Omega_M - \Omega_\Lambda$ (Carroll, Press and Turner 1992)². Observations of the CMB anisotropy (Spergel et al. 2003), high-redshift supernovae (Riess et al. 2004; Knop et al. 2003; Tonry et al. 2003) and mass measurements of galaxy clusters (e.g., Grego et al. 2001; Vikhlinin et al. 2003; Allen et al. 2004) indicate a flat, dark energy-dominated universe with $\Omega_M \simeq 0.3$ and $\Omega_\Lambda \simeq 0.7$, and these values are adopted in all subsequent analyses unless otherwise specified.

4.1. Measurement of the Hubble constant using the hydrostatic equilibrium model

We fit the theoretical $D_A(z)$ function to our sample of 38 cluster distances obtained with the hydrostatic equilibrium model. For the fit, we combine the statistical errors given in Table 3 with the data modelling D_A errors in Table 2, and obtain $H_0 = 76.9 \pm_{3.4}^{3.9}$ km s⁻¹ Mpc⁻¹ (68% confidence interval, statistical uncertainty only). The fit uses the MCMC parameter estimation method described in section 3.2, with the likelihood calculated using Equation 10. The χ^2 statistic of the best-fit model is 31.6 for 37 degrees of freedom.

²Throughout this paper, Ω_M , Ω_Λ , and Ω_k are defined at the present epoch (cf. Carroll, Press, and Turner 1992).

The total systematic errors in D_A are calculated by combining the individual systematic uncertainties of Table 3 in quadrature, applying the resulting errors to all 38 cluster distances, and repeating the fit. We obtain a systematic uncertainty in H_0 of $(+10.0, -8.0)$ km s $^{-1}$ Mpc $^{-1}$.

Figure 3 shows the Chandra/SZE cluster distance measurements, and the theoretical curve for the best-fit Hubble constant $H_0=76.9$ km s $^{-1}$ Mpc $^{-1}$ and $\Omega_M = 0.3$, $\Omega_\Lambda = 0.7$.

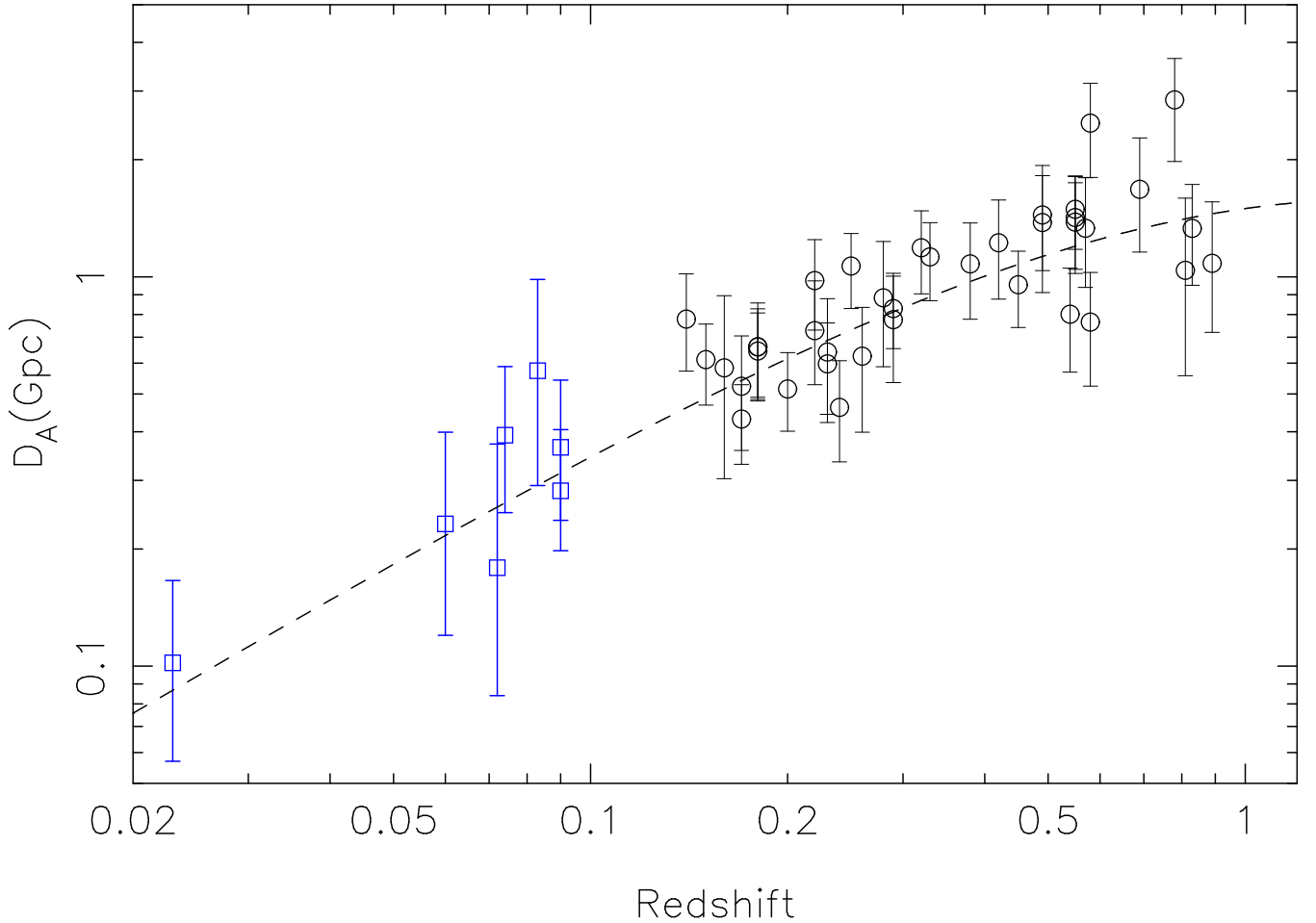


Fig. 3.— Angular diameter distances of the 38 clusters (open circles). The error bars are the total statistical uncertainties, obtained by combining the X-ray and SZE data modelling uncertainties (Table 2) and the additional sources of random error described in Section 3.3 and Table 3. The systematic errors of Table 3 are not shown. Dashed line is the angular diameter curve using the best-fit Hubble constant $H_0=76.9 \text{ km s}^{-1} \text{ Mpc}^{-1}$ and $\Omega_M = 0.3$, $\Omega_\Lambda = 0.7$. The open squares are from the low redshift sample of Mason et al. (2001), and they are not included in the fit.

We also show the angular diameter distances of nearby clusters from Mason et al. (2001), to demonstrate that the best-fit curve is in agreement with low-redshift X-ray/SZE measurements. Our measurement of H_0 in the distant universe is in agreement with the *Hubble Space Telescope* Key Project measurement of $H_0 = 72 \pm 8 \text{ km s}^{-1} \text{ Mpc}^{-1}$ (Freedman et al. 2001), which probes the nearby universe.

To address the effects of cosmology on the value of the Hubble constant obtained from the SZE/X-ray method, we also repeat the fit of our cluster distances varying the Ω_M and Ω_Λ in a fiducial interval around the currently favored ΛCDM model parameters, $\Omega_M = 0.2 - 0.4$ and $\Omega_\Lambda = 0.6 - 0.8$. The fits yield $H_0 = 78.8 \pm_{3.5}^{4.1}$ (68% statistical error), with a $\chi^2 = 31.9$ statistic for $\Omega_M = 0.2$, $\Omega_\Lambda = 0.8$, and $H_0 = 74.9 \pm_{3.2}^{3.8}$ ($\chi^2 = 31.5$) for $\Omega_M = 0.4$, $\Omega_\Lambda = 0.6$. Finally, we fit of our cluster distances with the theoretical $D_A(z)$ function for a matter-dominated universe with $\Omega_M = 1.0$ and $\Omega_\Lambda = 0.0$. The best-fit value of the Hubble constant in this case is $H_0 = 67.1 \pm_{3.6}^{4.5}$ (68% statistical error), with a χ^2 statistic of 32.5 for 37 degrees of freedom. These fits have the same quality as that for the currently favored $\Omega_M = 0.3$, $\Omega_\Lambda = 0.7$ cosmology, indicating that cluster distances alone can not yet effectively constrain the energy density parameters.

4.2. Measurement of the Hubble constant using the isothermal β -model

We compare the cluster distance results from the hydrostatic model of Section 4.1 to the results from other ICM models to determine how sensitive the distance measurements are to the details of the plasma modeling. These models consist of a simple isothermal β -model, with a density profile described by Equation 1 with $f=0$, and with a constant temperature. Since cluster centers often feature a sharp gradient in density and temperature, not consistent with this simple $f=0$ model, we also excised the central $r < 100 \text{ kpc}$ of the X-ray data from the analysis. Figure 2 and Table 7 show that, when the central 100 kpc are removed from the X-ray data, the temperature profiles out to $\sim 600 \text{ kpc}$ are essentially flat. With these simplifying assumptions, the X-ray surface brightness and SZE decrement have simple analytical functions (see, e.g., Birkinshaw et al. 1991), and numerical integrations are no longer needed. Also, we do not enforce hydrostatic equilibrium, and accordingly do not consider the dark matter distribution and the spectral likelihood information in the MCMC procedure described in Section 3.2.

There is no simple way to mask the central 100 kpc from our interferometric data, because these data are fit in the Fourier plane (La Roque 2005). However, the SZE data are less sensitive to the presence of a dense core than the X-ray data (Equation 4), and the X-ray data drive the fit for the density shape parameters. In addition, even clusters with X-ray

structures in the core are normally in pressure equilibrium (Markevitch et al. 2000, 2001), and should therefore have smooth SZE profiles. We therefore use the entire SZE dataset and the 100 kpc-cut X-ray dataset for this analysis. The assumptions of the model outlined above are described and tested in more detail in La Roque et al. (2006).

The model includes the following parameters: S_{X0} , r_c , β , ΔT_0 , kT and A , with the X-ray surface brightness S_X and the SZE decrement ΔT following the equations

$$S_X = S_{X0} \left(1 + \frac{r^2}{r_c^2} \right)^{(1-6\beta)/2} \quad (14)$$

$$\Delta T = \Delta T_0 \left(1 + \frac{r^2}{r_c^2} \right)^{(1-3\beta)/2} \quad (15)$$

The angular diameter distance D_A is calculated according to Equation 11, which is explained in detail in Bonamente et al. (2004). Applying this simple model to the data, we calculate the model parameters (Table 4) and the angular diameter distances (Figure 4). The same fitting technique employed in Section 4.1 above yields a best-fit Hubble constant of $H_0 = 77.6 \pm_{4.3}^{4.8} \pm_{8.2}^{10.1} \text{ km s}^{-1} \text{ Mpc}^{-1}$ (68% confidence interval, statistical followed by systematic errors), with a fit statistic of $\chi^2=53.9$ for 37 degrees of freedom. In this joint X-ray/SZE analysis, the spatial parameters S_{X0} , r_c , and β are constrained almost exclusively by the X-ray data, rather than by the SZE imaging, due to the high angular resolution and the large number of counts in the *Chandra*/ images. Constraints on ΔT_0 are obtained from the SZE data, while kT and A are obtained from the X-ray spectroscopy. The value of performing the joint MCMC analysis involving all three datasets is that the full probability density function for each model parameter can be obtained, with all statistically-allowable parameter variations included.

Finally, we include the results for the standard isothermal β model fit to the entire X-ray dataset, i.e., without the excision of the central 100 kpc. This exercise is provided for comparison with earlier analyses that used such modelling (e.g., Reese et al. 2002), and it is useful to assess the impact of the bright cluster cores on the determination of the distance scale. This model yields the best-fit parameters in Table 5, the angular diameter distances of Figure 4 and a best-fit Hubble constant of $H_0 = 73.7 \pm_{3.8}^{4.6} \pm_{7.6}^{9.5} \text{ km s}^{-1} \text{ Mpc}^{-1}$ (68% confidence interval, statistical followed by systematic errors), with a fit statistic of $\chi^2=53.1$ for 37 degrees of freedom.

These results indicate that the measurement of the cosmic distance scale using X-ray and SZE observations of galaxy clusters is insensitive to the details of the hot ICM model: the spread between the three models explored here is $3 \text{ km s}^{-1} \text{ Mpc}^{-1}$.

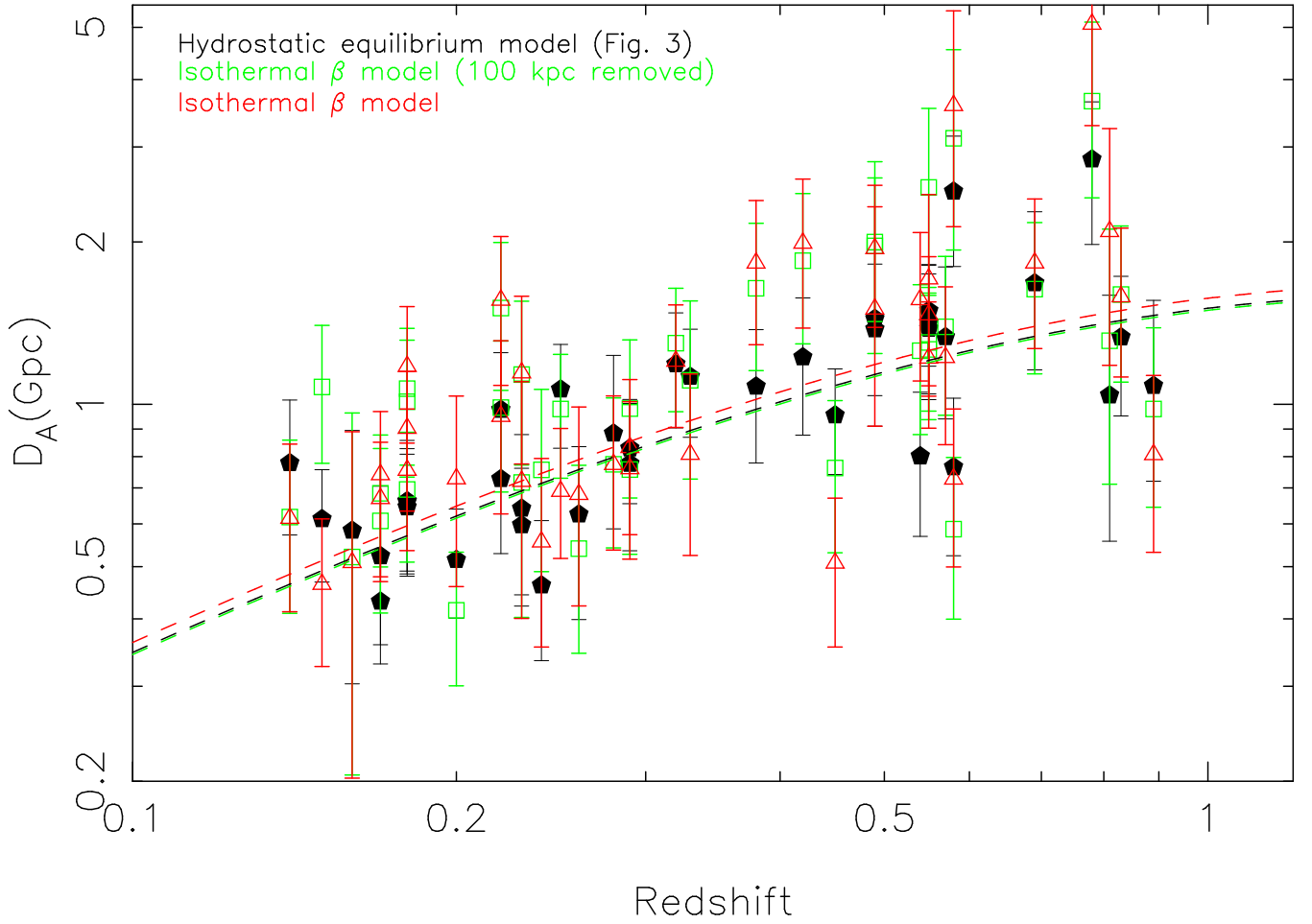


Fig. 4.— Angular diameter distances of the 38 clusters, using the simple $r < 100$ kpc-cut isothermal β model (green) and the isothermal β model (red) described in Section 4.2. The error bars are the total statistical uncertainties, obtained by adding the X-ray and SZE data modelling uncertainties (Table 4, Table 5) and the additional sources of random error described in Section 3.3 and Table 3. The systematic errors of Table 3 are not shown. Dashed lines are the best-fit angular diameter curves using the best-fit Hubble constant $H_0 = 77.6 \text{ km s}^{-1} \text{ Mpc}^{-1}$ (green) and $H_0 = 73.7 \text{ km s}^{-1} \text{ Mpc}^{-1}$ (red) and $\Omega_M = 0.3$, for $\Omega_\Lambda = 0.7$. In black are the distances obtained with the hydrostatic equilibrium model of Section 4.1 (Figure 3).

4.3. Comparison with recent distance measurements

We compare our results with recent X-ray/SZE measurements of the Hubble constant using clusters in our sample.

Jones et al. (2005), Saunders et al. (2003) and Grainge et al. (2002) use ROSAT and ASCA X-ray data and SZE data from the Ryle telescope for Abell 697, Abell 773, Abell 1413, Abell 1914 and Abell 2218. They employ an ellipsoidal β model to find $H_0 = 66 \pm 11 \pm 8$ km s $^{-1}$ Mpc $^{-1}$ for a Λ CDM cosmology, in agreement with our hydrostatic equilibrium model and our isothermal β model results.

Schmidt, Allen and Fabian (2004) use Chandra X-ray data and several published SZE measurements of RXJ1347.5-1145, Abell 1835 and Abell 478 (the latter not included in our sample), and employ a hydrostatic equilibrium model similar to the one used in this paper. They obtain a best-fit $H_0 = 69 \pm 8$ km s $^{-1}$ Mpc $^{-1}$ for a Λ CDM cosmology, also in agreement with our hydrostatic equilibrium model results.

Worrall and Birkinshaw (2003) use a β model fit to the XMM-Newton X-ray data and the Hughes and Birkinshaw (1998) SZE data of CL0016+1609 to find a best-fit $D_A = 1.36 \pm 0.15$ Gpc. This measurement is in excellent agreement with our hydrostatic equilibrium model for this cluster ($D_A = 1.38 \pm 0.22$ Gpc, Table 2) and isothermal β models ($D_A = 1.22 \pm 0.21$ Gpc, Table 4; $D_A = 1.30 \pm 0.19$ Gpc, Table 5).

5. Conclusions

We analyzed 38 clusters of galaxies with *Chandra* X-ray imaging spectroscopy and *OVRO-BIMA* SZE data, the largest sample to date used to measure H_0 . We applied a hydrostatic equilibrium model that accounts for radial variations in cluster temperature, and for sharp density gradients caused by the cooling of the plasma in the cluster core. The joint analysis of X-ray and SZE data yields a direct measurement of the cosmic distance scale in the redshift range $0.14 < z < 0.89$. We measure a Hubble constant of $H_0 = 76.9 \pm_{3.4}^{3.9} \pm_{8.0}^{10.0}$ km s $^{-1}$ Mpc $^{-1}$ for an $\Omega_M = 0.3$, $\Omega_\Lambda = 0.7$ cosmology (68 % confidence interval, statistical followed by systematic uncertainty), which is in agreement with the *Hubble Space Telescope* Key Project results obtained at low redshift. We also analyze our measurements with a simple isothermal model of the hot plasma without the hydrostatic equilibrium assumption. The results from this simple model are in good agreement with the hydrostatic equilibrium model, indicating that the X-ray/SZE method used to determine the cosmic distance scale is largely insensitive to the details of the hot plasma modeling.

Acknowledgments:

This paper is dedicated to Leon van Speybroeck and his colleagues on the *Chandra* project, including H. Ebeling, W. Forman, J.P. Hughes, C. Jones, M. Markevitch, H. Tananbaum, A. Vikhlinin and M. Weisskopf; without their effort to construct an exceptional observatory and to obtain deep observations of a large number of clusters, this research would not have been possible. The support of the BIMA and OVRO staff over many years is also gratefully acknowledged, including J.R. Forster, C. Giovanine, R. Lawrence, S. Padin, R. Plambeck, S. Scott and D. Woody. We thank C. Alexander, K. Coble, A. Cooray, L. Grego, G. Holder, W. Holzapfel, A. Miller, J. Mohr, D. Nagai, S. Patel and P. Whitehouse for their outstanding contributions to the SZE instrumentation, observations, and analysis. We also thank J. Mohr and D. Nagai for contributions to the development of the hydrostatic equilibrium model.

This work was supported by NASA LTSA grant NAG5-7985 and also in part by NSF grants PHY-0114422 and AST-0096913, the David and Lucile Packard Foundation, the McDonnell Foundation, and a MSFC director's discretionary award. Research at the Owens Valley Radio Observatory and the Berkeley-Illinois-Maryland Array was supported by National Science Foundation grants AST 99-81546 and 02-28963. Calculations were performed at the Space Plasma Interactive Data Analysis and Simulation Laboratory at the Center for Space Plasma and Aeronomy Research of the University of Alabama at Huntsville.

REFERENCES

- Allen, S. W. et al. 1992, MNRAS, 259, 67
Allen, S. W. et al. 2004, MNRAS, 353, 457
Birkinshaw, M., Hughes, J.P. and Arnaud, K.A. 1991, ApJ, 379, 466
Birkinshaw, M. and Hughes, J.P. 1994, ApJ, 420, 33
Böhringer, H. et al. 2000, ApJS, 129, 435
Bonamente, M., Joy, M., Carlstrom, J., Reese, E. and La Roque, S. 2004, ApJ, 614, 56
Carlstrom, J.E., Joy, M.K. and Grego, L. 1996, ApJ, 456, 75
Carlstrom, J.E., Holder, G.P. and Reese, E.D. 2002, ARA&A, 40, 643
Carroll, S., Press, W. and Turner, E. 1992, ARA&A, 30, 499

- Cavaliere, A. and Fusco-Femiano, R. 1976, A&A, 49, 137
- Chandra Proposers Observatory Guide, <http://asc.harvard.edu/proposer/POG/html>
- Colberg, J.M. et al. 2000, MNRAS, 313, 229
- Dawson, K. S., Holzapfel, W.L., Carlstrom, J.E., Joy, M.K., LaRoque, S.J. and Reese, E.D. 2001, ApJ, 553, 1
- Dawson, K. S., Holzapfel, W.L., Carlstrom, J.E., Joy, M.K. and LaRoque 2006, ApJ submitted (astro-ph/0602413)
- De Grandi, S. and Molendi, S. 2001, ApJ, 551, 153
- De Grandi, S. and Molendi, S. 2002, ApJ, 567, 163
- De Grandi, S., Ettori, S., Longhetti, M. and Molendi, S. 2004, A&A, 419, 7
- Dickey, J.M. and Lockman, F.J. 1990, ARA&A, 28, 215
- Donahue, M., Voit, G. M., Scharf, C. A., Gioia, I. M., Mullis, C. R., Hughes, J. P., & Stocke, J. T. 1999, ApJ, 527, 525
- Ebeling, H., Jones, L. R., Fairley, B. W., Perlman, E., Scharf, C., & Horner, D. 2001b, ApJ, 548, L23
- Ebeling, H., Edge, A. C., Bohringer, H., Allen, S. W., Crawford, C. S., Fabian, A. C., Voges, W., & Huchra, J. P. 1998, MNRAS, 301, 881
- Efstathiou, G., and Bond, J.R., 1999, MNRAS304, 75
- Feretti, L. 2004, in X-Ray and Radio Connections, Eds. L.O. Sjouwerman and K.K Dyer, <http://www.aoc.nrao.edu/events/xraydio>
- Fixsen, D.J. et al. 1996, ApJ, 473, 576
- Freedman, W. et al. 2001, ApJ, 553, 47
- Gamerman, D. 1997, Markov Chain Monte Carlo: stochastic simulation for Bayesian inference, Chapman and Hall
- Gelman, A. and Rubin D.B. 1992, Stat. Science 7, 457
- Gelman, A. 1996, in Markov Chain Monte Carlo in practice, Eds. Gilks, W.R., Richardson, S. and Spiegelhalter, D.J. , p. 131.

- Geweke, J. 1992, in Bayesian Statistics IV, Ed. Bernardo, J.M. e al., Clarendon Press-Oxford, 169
- Gioia, I. M., & Luppino, G. A. 1994, ApJS, 94, 583
- Gilks, W.R., Richardson, S. and Spiegelhalter, D.J. 1996, Markov Chain Monte Carlo in practice, Chapman and Hall
- Giovannini, G. and Feretti, L. 2004, JKAS 37, 328
- Grainge, K., Jones, M., Pooley, G., Saunders, R. and Edge, A. 1993, MNRAS, 265, 57
- Grainge, K. et al. 2002, MNRAS, 333, 318
- Grego, L. et al. 2000, ApJ, 539, 39
- Grego, L. et al. 2001, ApJ, 552, 2
- Hastings, W.K. 1970, Biometrika, 57, 97
- Henry, J. P. et al. 1997, AJ, 114, 1293
- Herbig, T., Lawrence, C. R., Readhead, A. C. S. and Gulkis, S. 1995, ApJ, 449, 5
- Holzapfel, W. L., Arnaud, M., Ade, P. A. R., Church, S. E., Fischer, M. L., Mauskopf, P. D., Rephaeli, Y., Wilbanks, T. M. and Lange, A. E. 1997a, ApJ, 480, 449
- Holzapfel, W. L., Wilbanks, T. M., Ade, P. A. R., Church, S. E., Fischer, M. L., Mauskopf, P. D., Osgood, D. E. and Lange, A. E. 1997b, ApJ, 479, 17
- Holzapfel, W. L., Carlstrom, J. E., Grego, L., Holder, G., Joy, M. and Reese, E. D. 2000, ApJ539, 57
- Hughes, J.P. and Birkinshaw, M. 1998, ApJ, 501, 1
- Jeltema, T. E., Canizares, C. R., Bautz, M. W. and Buote, David A. 2005, ApJ, 624, 606
- Jones, M.E. et al. 1993, Nature, 365, 320
- Jones, M. et al. 2005, MNRAS, 357, 518
- Knop, R.A. et al. 2003, ApJ, 598, 102
- Komatsu, E. Kitayama, T. Suto, Y., Hattori, M., Kawabe, R. Matsuo, H., Schindler, S. and Yoshikawa, K. 1999, ApJ, 516, 1

- Lamarre, J.M. et al. 1998, ApJ, 507, 5
- LaRoque, S. J. et al. 2003, ApJ, 583, 559
- La Roque, S. 2005, Ph.D. Thesis, the University of Chicago
- La Roque, S., Bonamente, M., Joy, M., Carlstrom, J., Nagai, D., Reese, E. and Dawson, K. 2006, ApJ, in preparation
- Luppino, G. A., Gioia, I. M. 1995, ApJ, 445, 77
- Mason, B., Myers, S and Redhead, A. 2001, ApJ, 555, 11
- Metropolis, N., Rosenbluth, A.W., Rosenbluth, M.N., Teller, A.H. and Teller, E. 1953, Journal of Chemical Physics, 21, 1087
- Mohr, J., Mathiesen, B. and Evrard, A. 1999, ApJ, 517, 627
- Myers, S. T., Baker, J. E., Readhead, A. C. S., Leitch, E. M. and Herbig, T. 1997, ApJ, 485, 1
- Navarro, J., Frenk, C. and White, S. 1997, ApJ, 490, 493
- Pearson, T.J., Shepherd, M.C., Taylor, G.B. and Meyers, S.T. 1994, BAAS, 185, 808
- Patel, S. K. et al. 2000, ApJ, 541, 37
- Pointecouteau, E., Giard, M., Benoit, A., Desert, F. X., Aghanim, N., Coron, N., Lamarre, J. M. and Delabrouille, J. 1999, ApJ, 519, 115
- Pointecouteau, E., Giard, M., Benoit, A., Desert, F. X., Bernard, J. P., Coron, N. and Lamarre, J. M. 2001, ApJ, 552, 42
- Raftery, A.L. and Lewis, S. 1992, 763, Bayesian Statistic 4, Eds. J.M. Bernardo et al., Oxford University Press
- Reese, E.D. et al. 2000, ApJ, 533, 38
- Reese, E.D., Carlstrom, J.E., Joy, M.K., Mohr, J.J., Grego, L. and Holzapfel, W.L. 2002, ApJ, 581, 53
- Reese, E. 2004, ‘Measuring and Modeling the Universe’, Cambridge Univ. Press, Ed. W. Freedman, p. 138
- Riess, A.G. et al. 2004, ApJ, 607, 665

- Riess, A.G. et al. 2005, ApJ, 627, 579
- Roberts, G.O. 1996, in Markov Chain Monte Carlo in practice, Ed.s Gilks, W.R., Richardson, S. and Spiegelhalter, D.J., Chapman and Hall, 45.
- Sarazin, C. 1988, ‘X-ray emission from clusters of galaxies’, Cambridge University Press.
- Sault, R.J., Teuben, P.J. and Wright, M.C. 1995, in ASP Conf. Ser. 77, AStrominical Data Analysis Software and Systems IV, ed. R.A. Shaw, H.E. Paine and J.J.E. Hayes (San Francisco:ASP), 433
- Saunders, R. et al. 2003, MNRAS, 341, 937
- Schindler, S. et al. 1995, A&A, 299, L9
- Schmidt, R.W., Allen, S.W. and Fabian, A.C. 2004, MNRAS, 352, 1413
- Scoville, N.Z. et al. 1993, PASP, 105, 1482
- Snowden, S.L., Egger, R., Finkbeiner, D.P., Freyberg, M.J. and Plucinsky, P.P. 1998, ApJ, 493, 715
- Spergel, D. et al. 2003, ApJS, 148, 175
- Stocke, J. T., Morris, S. L., Gioia, I. M., Maccacaro, T., Schild, R., Wolter, A., Fleming, T. A., & Henry, J. P. 1991, ApJS, 76, 813
- Struble, M. F., & Rood, H. J. 1999, ApJS, 125, 35
- Sulkanen, M. E. 1999, ApJ, 522, 59
- Sunyaev, R.A. and Zel'dovich, Y.B. 1970, Comments Astrophys. Space Phys., 2, 66
- Sunyaev, R.A. and Zel'dovich, Y.B. 1972, Comments Astrophys. Space Phys., 4, 173
- Tonry, L. et al. 2003, ApJ, 594, 1
- Udomprasert, P. S., Mason, B. S., Readhead, A. C. S. and Pearson, T. J. 2004, ApJ, 615, 63
- Verde, L. et al. 2003, ApJS, 148, 195
- Vikhlinin, A. et al. 2003, ApJ, 590, 15
- Worrall, D.M. and Birkinshaw, M. 2003, MNRAS, 340, 1261
- Watkins, R. 1997, MNRAS, 292, 59

Table 1. Cluster Data

Cluster	z	Chandra X-ray Data						Interferometric SZE Data					z reference
		ObsID	Chip	(ks)	(hh mm ss)	(\circ $'$ $''$)	BIMA (hr)	OVRO (hr)	(hh mm ss)	(\circ $'$ $''$)			
CL 0016+1609	0.541	520	I3	67.4	00 18 33.5	+16 26 12.5	43	100	00 18 33.3	+16 26 04.0	Stocke et al. (1991)		
Abell 68	0.255	3250	I3	10.0	00 37 06.2	+09 09 33.2	54	—	00 37 04.0	+09 10 02.5	Struble & Rood (1999)		
Abell 267	0.230	1448	I3	7.4	01 52 42.1	+01 00 35.7	50	—	01 52 42.3	+01 00 26.0	Struble & Rood (1999)		
Abell 370	0.375	515	S3	65.3	02 39 53.2	-01 34 35.0	26	33	02 39 52.4	-01 34 43.8	Struble & Rood (1999)		
MS 0451.6-0305	0.550	902	S3	42.2	04 54 11.4	-03 00 52.7	—	30	04 54 11.6	-03 01 01.3	Gioia & Luppino (1994)		
		529	I3	13.9									
MACS J0647.7+7015	0.584	3196	I3	19.3	06 47 50.2	+70 14 54.6	—	23	06 47 50.2	+70 14 56.1	LaRoque et al. (2003)		
		3584	I3	20.0									
Abell 586	0.171	530	I3	10.0	07 32 20.2	+31 37 55.6	45	—	07 32 19.6	+31 37 55.3	Struble & Rood (1999)		
MACS J0744.8+3927	0.686	3197	I3	20.2	07 44 52.8	+39 27 26.7	8	17	07 44 52.4	+39 27 33.2	LaRoque et al. (2003)		
		3585	I3	19.4									
Abell 611	0.288	3194	S3	36.1	08 00 56.6	+36 03 24.1	—	57	08 00 56.5	+36 03 22.9	Struble & Rood (1999)		
Abell 665	0.182	3586	I3	29.7	08 30 58.1	+65 50 51.6	52	16	08 30 58.6	+65 50 49.8	Struble & Rood (1999)		
		531	I3	9.0									
Abell 697	0.282	4217	I3	19.5	08 42 57.5	+36 21 56.2	—	47	08 42 57.8	+36 21 54.5	Struble & Rood (1999)		
Abell 773	0.217	533	I3	11.3	09 17 52.8	+51 43 38.9	26	66	09 17 53.5	+51 43 49.8	Struble & Rood (1999)		
		3588	I3	9.4									
ZW 3146	0.291	909	I3	46.0	10 23 39.7	+04 11 09.5	25	15	10 23 37.8	+04 11 17.8	Allen et al. (1992)		
MS 1054.5-0321	0.826	512	S3	89.1	10 56 59.4	-03 37 34.2	—	43	10 56 59.1	-03 37 34.0	Luppino & Gioia (1995)		
MS 1137.5+6625	0.784	536	I3	77.0	11 40 22.3	+66 08 16.0	88	—	11 40 23.1	+66 08 05.3	Donahue et al. (1999)		
MACS J1149.5+2223	0.544	1656	I3	18.5	11 49 35.5	+22 24 02.3	39	—	11 49 34.9	+22 23 54.8	LaRoque et al. (2003)		
		3589	I3	20.0									
Abell 1413	0.142	1661	I3	9.7	11 55 18.0	+23 24 17.0	28	—	11 55 17.7	+23 24 39.5	Struble & Rood (1999)		
		537	I3	9.6									
CL J1226.9+3332	0.890	3180	I3	31.7	12 26 57.9	+33 32 47.4	33	—	12 26 58.0	+33.32 57.9	Ebeling et al. (2001b)		
		932	S3	9.9									
MACS J1311.0-0310	0.490	3258	I3	14.9	13 11 01.7	-03 10 38.5	39	—	13 11 02.2	-03 10 45.6	Allen et al. (2004)		
Abell 1689	0.183	1663	I3	10.7	13 11 29.5	-01 20 28.2	16	26	13 11 29.1	-01 20 29.7	Struble & Rood (1999)		
		540	I3	10.3									
RX J1347.5-1145	0.451	3592	I3	57.7	13 47 30.6	-11 45 08.6	22	3	13 47 30.6	-11 45 12.3	Schindler et al. (1995)		
MS 1358.4+6245	0.327	516	S3	48.1	35 59 50.6	+62 31 04.1	70	—	13 59 50.2	+62 31 07.0	Gioia & Luppino (1994)		
Abell 1835	0.252	495	S3	19.5	14 01 02.0	+02 52 41.7	27	23	14 01 01.8	+02 52 45.6	Struble & Rood (1999)		
		496	S3	10.7									
MACS J1423.8+2404	0.545	4195	S3	115.6	14 23 47.9	+24 04 42.6	35	—	14 23 47.7	+24 04 37.3	LaRoque et al. (2003)		
Abell 1914	0.171	3593	I3	18.9	14 26 00.8	+37 49 35.7	24	—	14 26 01.3	37 49 38.6	Struble & Rood (1999)		

Table 1—Continued

Cluster	z	Chandra X-ray Data						Interferometric SZE Data					z reference
		ObsID	Chip	(ks)	(hh mm ss)	(\circ $'$ $''$)	BIMA (hr)	OVRO (hr)	(hh mm ss)	(\circ $'$ $''$)			
		542	I3	8.1									
Abell 1995	0.322	906	S3	56.7	14 52 57.9	+58 02 55.8	50	58	14 52 58.1	+58 02 57.0		Patel et al. (2000)	
Abell 2111	0.229	544	I3	10.3	15 39 41.0	+34 25 08.8	36	—	15 39 40.2	+34 25 00.4		Struble & Rood (1999)	
Abell 2163	0.202	1653	I1	71.1	16 15 46.2	-06 08 51.3	23	37	16 15 43.6	-06 08 46.6		Struble & Rood (1999)	
Abell 2204	0.152	499	S3	8.6	16 32 46.9	+05 34 31.9	30	—	16 32 46.6	+05 34 20.6		Struble & Rood (1999)	
		6104	I3	9.6									
Abell 2218	0.176	1666	I0	41.7	16 35 51.9	+66 12 34.5	32	70	16 35 48.7	+66 12 28.1		Struble & Rood (1999)	
RX J1716.4+6708	0.813	548	I3	51.7	17 16 48.8	+67 08 25.3	37	—	17 16 51.2	+67 07 49.6		Henry et al. (1997)	
Abell 2259	0.164	3245	I3	10.0	17 20 08.5	+27 40 11.0	25	—	17 20 09.0	+27 40 09.4		Struble & Rood (1999)	
Abell 2261	0.224	550	I3	9.1	17 22 27.1	+32 07 57.8	23	40	17 22 26.9	+32 07 59.9		Struble & Rood (1999)	
MS 2053.7-0449	0.583	551	I3	44.3	20 56 21.2	-04 37 47.8	—	154	20 56 21.0	-04 37 47.2		Stocke et al. (1991)	
		1667	I3	44.5									
MACS J2129.4-0741	0.570	3199	I3	8.5	21 29 26.0	-07 41 28.7	—	24	21 29 24.9	-07 41 43.9		LaRoque et al. (2003)	
		3595	I3	18.4									
RX J2129.7+0005	0.235	552	I3	10.0	21 29 39.9	+00 05 19.8	47	—	21 29 38.1	+00 05 12.4		Ebeling et al. (1998)	
MACS J2214.9-1359	0.483	3259	I3	19.5	22 14 57.3	-14 00 12.3	41	11	22 14 58.4	-14 00 10.9		Note (^a)	
		5011	I3	16.1									
MACS J2228.5+2036	0.412	3285	I3	19.9	22 28 33.0	+20 37 14.4	39	—	22 28 33.1	+20 37 14.2		Böhringer et al. (2000)	

^aRedshift derived from the Fe lines in the Chandra x-ray spectrum, this paper.

Table 2. Results of the hydrostatic equilibrium model

Cluster	\mathcal{N} (10^{-25} g cm $^{-3}$)	r_s (arcsec)	n_{e0} (cm $^{-3}$)	r_{c1} (arcsec)	β	f	r_{c2} (arcsec)	D_A Gpc
CL 0016+1609	$0.10^{+0.14}_{-0.06}$	225^{+233}_{-96}	$1.40^{+0.18}_{-0.15} \times 10^{-2}$	$10.3^{+4.4}_{-2.5}$	$0.761^{+0.031}_{-0.036}$	$0.48^{+0.05}_{-0.05}$	$47.8^{+3.8}_{-3.7}$	$1.38^{+0.22}_{-0.22}$
Abell 0068	$3.29^{+7.60}_{-2.51}$	70^{+62}_{-27}	$8.89^{+1.68}_{-1.18} \times 10^{-3}$	—	$0.693^{+0.026}_{-0.028}$	—	$47.8^{+2.8}_{-3.0}$	$0.63^{+0.16}_{-0.19}$
Abell 0267	$2.02^{+3.04}_{-1.24}$	75^{+50}_{-31}	$1.17^{+0.11}_{-0.10} \times 10^{-2}$	—	$0.698^{+0.031}_{-0.030}$	—	$40.9^{+2.8}_{-2.8}$	$0.60^{+0.11}_{-0.09}$
Abell 0370	$1.63^{+1.80}_{-0.87}$	51^{+21}_{-13}	$5.33^{+0.58}_{-0.40} \times 10^{-3}$	—	$0.740^{+0.035}_{-0.028}$	—	$55.6^{+3.1}_{-2.6}$	$1.08^{+0.19}_{-0.20}$
MS 0451.6-0305	$0.27^{+0.58}_{-0.16}$	110^{+75}_{-44}	$1.26^{+0.12}_{-0.09} \times 10^{-2}$	—	$0.777^{+0.019}_{-0.019}$	—	$34.5^{+1.1}_{-1.1}$	$1.42^{+0.26}_{-0.23}$
MACS J0647.7+7015	$12.01^{+16.67}_{-8.41}$	36^{+22}_{-13}	$2.19^{+0.34}_{-0.25} \times 10^{-2}$	—	$0.653^{+0.019}_{-0.017}$	—	$19.9^{+1.2}_{-1.2}$	$0.77^{+0.21}_{-0.18}$
Abell 0586	$1.78^{+1.97}_{-1.05}$	102^{+40}_{-26}	$1.83^{+0.25}_{-0.21} \times 10^{-2}$	—	$0.627^{+0.017}_{-0.013}$	—	$32.0^{+1.7}_{-1.4}$	$0.52^{+0.15}_{-0.12}$
MACS J0744.8+3927	$0.27^{+0.84}_{-0.22}$	94^{+102}_{-51}	$1.14^{+0.22}_{-0.15} \times 10^{-1}$	$3.4^{+0.6}_{-0.7}$	$0.635^{+0.049}_{-0.039}$	$0.93^{+0.01}_{-0.01}$	$25.8^{+4.7}_{-4.7}$	$1.68^{+0.48}_{-0.38}$
Abell 0611	$1.73^{+1.87}_{-0.90}$	64^{+15}_{-12}	$5.27^{+0.97}_{-0.90} \times 10^{-2}$	$2.8^{+0.4}_{-0.3}$	$0.600^{+0.014}_{-0.008}$	$0.66^{+0.08}_{-0.07}$	$22.5^{+1.6}_{-1.2}$	$0.78^{+0.18}_{-0.18}$
Abell 0665	$0.18^{+0.14}_{-0.09}$	340^{+150}_{-86}	$9.13^{+1.34}_{-1.06} \times 10^{-3}$	$3.2^{+0.8}_{-0.5}$	$0.730^{+0.015}_{-0.016}$	$0.11^{+0.10}_{-0.08}$	$64.4^{+1.7}_{-1.7}$	$0.66^{+0.09}_{-0.10}$
Abell 0697	$0.76^{+1.63}_{-0.59}$	93^{+66}_{-32}	$9.82^{+1.55}_{-1.28} \times 10^{-3}$	—	$0.584^{+0.014}_{-0.016}$	—	$41.6^{+1.8}_{-1.9}$	$0.88^{+0.30}_{-0.23}$
Abell 0773	$1.22^{+1.98}_{-0.88}$	54^{+40}_{-19}	$8.04^{+0.68}_{-0.64} \times 10^{-3}$	—	$0.564^{+0.020}_{-0.022}$	—	$40.2^{+2.2}_{-2.2}$	$0.98^{+0.17}_{-0.14}$
ZW 3146	$0.66^{+0.08}_{-0.05}$	121^{+4}_{-6}	$1.70^{+0.02}_{-0.03} \times 10^{-1}$	$4.4^{+0.1}_{-0.1}$	$0.668^{+0.005}_{-0.004}$	$0.881^{+0.004}_{-0.003}$	$25.5^{+0.3}_{-0.4}$	$0.83^{+0.02}_{-0.02}$
MS 1054-0321	$0.04^{+0.08}_{-0.02}$	666^{+571}_{-359}	$6.15^{+0.71}_{-0.56} \times 10^{-3}$	—	$1.791^{+0.148}_{-0.209}$	—	$83.7^{+4.9}_{-7.3}$	$1.33^{+0.28}_{-0.26}$
MS 1137.5+6625	$1.73^{+3.31}_{-1.40}$	16^{+18}_{-9}	$1.26^{+0.16}_{-0.11} \times 10^{-2}$	—	$0.667^{+0.044}_{-0.043}$	—	$14.2^{+1.3}_{-1.3}$	$2.85^{+0.52}_{-0.52}$
MACS J1149.5+2223	$0.74^{+3.06}_{-0.50}$	110^{+46}_{-29}	$8.53^{+0.04}_{-0.89} \times 10^{-3}$	—	$0.673^{+0.020}_{-0.022}$	—	$42.8^{+2.1}_{-2.4}$	$0.80^{+0.19}_{-0.16}$
Abell 1413	$0.47^{+0.58}_{-0.27}$	121^{+51}_{-47}	$3.66^{+0.65}_{-0.42} \times 10^{-2}$	$6.5^{+1.5}_{-1.3}$	$0.531^{+0.018}_{-0.014}$	$0.76^{+0.02}_{-0.02}$	$39.3^{+4.5}_{-3.7}$	$0.78^{+0.18}_{-0.13}$
CL J1226.9+3332	$4.09^{+9.41}_{-3.58}$	46^{+58}_{-19}	$3.01^{+0.47}_{-0.44} \times 10^{-2}$	—	$0.715^{+0.038}_{-0.038}$	—	$15.8^{+1.3}_{-1.4}$	$1.08^{+0.42}_{-0.28}$
MACS J1311.0-0310	$7.59^{+17.81}_{-7.09}$	19^{+47}_{-9}	$3.93^{+0.72}_{-0.55} \times 10^{-2}$	—	$0.613^{+0.022}_{-0.020}$	—	$9.3^{+0.7}_{-0.7}$	$1.38^{+0.47}_{-0.37}$
Abell 1689	$2.68^{+1.20}_{-1.16}$	75^{+19}_{-10}	$4.054^{+0.36}_{-0.26} \times 10^{-2}$	$21.7^{+0.9}_{-1.0}$	$0.873^{+0.039}_{-0.041}$	$0.87^{+0.01}_{-0.01}$	$104.9^{+5.1}_{-5.5}$	$0.65^{+0.09}_{-0.09}$
RX J1347.5-1145	$4.57^{+1.06}_{-0.86}$	47^{+5}_{-5}	$2.81^{+0.16}_{-0.12} \times 10^{-1}$	$3.9^{+0.2}_{-0.1}$	$0.631^{+0.009}_{-0.008}$	$0.942^{+0.004}_{-0.004}$	$22.9^{+1.8}_{-1.4}$	$0.96^{+0.06}_{-0.08}$
MS 1358.4+6245	$0.58^{+0.21}_{-0.19}$	90^{+26}_{-18}	$9.62^{+0.79}_{-0.78} \times 10^{-2}$	$3.3^{+0.2}_{-0.2}$	$0.675^{+0.017}_{-0.016}$	$0.934^{+0.003}_{-0.003}$	$37.2^{+1.7}_{-1.9}$	$1.13^{+0.09}_{-0.10}$
Abell 1835	$0.28^{+0.10}_{-0.03}$	150^{+11}_{-11}	$1.10^{+0.05}_{-0.02} \times 10^{-1}$	$9.3^{+0.2}_{-0.2}$	$0.798^{+0.013}_{-0.017}$	$0.940^{+0.001}_{-0.001}$	$63.7^{+1.5}_{-1.6}$	$1.07^{+0.02}_{-0.08}$
MACS J1423.8+2504	$1.83^{+0.02}_{-0.07}$	33^{+1}_{-1}	$1.60^{+0.02}_{-0.08} \times 10^{-1}$	$4.2^{+0.1}_{-0.1}$	$0.721^{+0.012}_{-0.008}$	$0.975^{+0.001}_{-0.001}$	$36.7^{+0.9}_{-0.7}$	$1.49^{+0.06}_{-0.03}$
Abell 1914	$5.79^{+2.60}_{-1.85}$	81^{+14}_{-11}	$1.72^{+0.13}_{-0.08} \times 10^{-2}$	$6.6^{+0.6}_{-0.8}$	$0.899^{+0.007}_{-0.012}$	$0.008^{+0.018}_{-0.008}$	$68.3^{+0.7}_{-1.0}$	$0.44^{+0.04}_{-0.05}$
Abell 1995	$0.07^{+0.06}_{-0.04}$	359^{+205}_{-117}	$9.35^{+0.74}_{-0.56} \times 10^{-3}$	$31.2^{+3.0}_{-3.5}$	$1.298^{+0.062}_{-0.096}$	$0.462^{+0.033}_{-0.033}$	$83.5^{+3.7}_{-7.1}$	$1.19^{+0.15}_{-0.14}$
Abell 2111	$0.47^{+2.74}_{-0.38}$	172^{+354}_{-107}	$5.99^{+1.05}_{-0.79} \times 10^{-3}$	—	$0.600^{+0.026}_{-0.025}$	—	$50.4^{+3.8}_{-3.5}$	$0.64^{+0.20}_{-0.17}$
Abell 2163	$0.26^{+0.12}_{-0.09}$	390^{+87}_{-52}	$1.09^{+0.07}_{-0.04} \times 10^{-2}$	$4.0^{+1.3}_{-0.7}$	$0.560^{+0.004}_{-0.005}$	$0.022^{+0.037}_{-0.022}$	$66.8^{+0.9}_{-0.8}$	$0.52^{+0.04}_{-0.05}$
Abell 2204	$0.92^{+0.30}_{-0.15}$	120^{+13}_{-18}	$2.01^{+0.12}_{-0.09} \times 10^{-1}$	$7.5^{+0.3}_{-0.3}$	$0.710^{+0.031}_{-0.025}$	$0.960^{+0.003}_{-0.004}$	$67.4^{+2.0}_{-1.8}$	$0.61^{+0.06}_{-0.07}$
Abell 2218	$1.02^{+0.70}_{-0.60}$	110^{+35}_{-22}	$7.02^{+0.66}_{-0.66} \times 10^{-3}$	—	$0.739^{+0.014}_{-0.017}$	—	$68.3^{+1.7}_{-2.1}$	$0.66^{+0.14}_{-0.11}$
RX J1716.4+6708	$0.34^{+3.38}_{-0.30}$	146^{+545}_{-106}	$1.94^{+0.61}_{-0.40} \times 10^{-2}$	—	$0.589^{+0.042}_{-0.035}$	—	$12.3^{+2.0}_{-1.7}$	$1.04^{+0.51}_{-0.43}$
Abell 2259	$0.65^{+1.15}_{-0.54}$	141^{+155}_{-56}	$9.29^{+2.97}_{-1.71} \times 10^{-3}$	—	$0.560^{+0.025}_{-0.024}$	—	$41.0^{+3.9}_{-2.8}$	$0.58^{+0.29}_{-0.25}$
Abell 2261	$1.36^{+0.85}_{-0.85}$	68^{+25}_{-15}	$4.16^{+0.54}_{-0.63} \times 10^{-2}$	$10.0^{+1.9}_{-1.7}$	$0.628^{+0.025}_{-0.022}$	$0.77^{+0.04}_{-0.05}$	$37.8^{+6.0}_{-5.2}$	$0.73^{+0.20}_{-0.13}$
MS 2053.7-0449	$0.26^{+1.41}_{-0.22}$	40^{+64}_{-22}	$9.22^{+1.08}_{-0.92} \times 10^{-3}$	—	$0.522^{+0.048}_{-0.042}$	—	$10.8^{+1.5}_{-1.7}$	$2.48^{+0.41}_{-0.44}$
MACS J2129.4-0741	$6.05^{+17.17}_{-5.15}$	20^{+23}_{-8}	$1.71^{+0.19}_{-0.19} \times 10^{-2}$	—	$0.626^{+0.027}_{-0.029}$	—	$19.7^{+1.5}_{-1.5}$	$1.33^{+0.37}_{-0.28}$
RX J2129.7+0005	$3.04^{+1.66}_{-1.41}$	84^{+21}_{-15}	$1.78^{+0.22}_{-0.21} i \times 10^{-1}$	$3.6^{+0.5}_{-0.4}$	$0.588^{+0.012}_{-0.015}$	$0.91^{+0.01}_{-0.01}$	$26.1^{+3.0}_{-2.9}$	$0.46^{+0.11}_{-0.08}$

Table 2—Continued

Cluster	\mathcal{N} (10^{-25} g cm $^{-3}$)	r_s (arcsec)	n_{e0} (cm $^{-3}$)	r_{c1} (arcsec)	β	f	r_{c2} (arcsec)	D_A Gpc
MACS J2214.9-1359	$0.66^{+1.40}_{-0.51}$	64^{+62}_{-32}	$1.35^{+0.13}_{-0.13} \times 10^{-2}$	—	$0.615^{+0.016}_{-0.020}$	—	$22.8^{+1.2}_{-1.3}$	$1.44^{+0.27}_{-0.23}$
MACS J2228.5+2036	$0.41^{+1.12}_{-0.32}$	101^{+108}_{-45}	$1.24^{+0.14}_{-0.11} \times 10^{-2}$	—	$0.519^{+0.014}_{-0.013}$	—	$21.7^{+1.4}_{-1.3}$	$1.22^{+0.24}_{-0.23}$

Table 3. Sources of uncertainty in the measurement of D_A

Source	Effect on D_A	Reference
STATISTICAL CONTRIBUTIONS		
Galactic N_H	$\leq \pm 1\%$	(1)
Cluster asphericity	$\pm 15\%$	(2)
SZE point sources	$\pm 8\%$	(3)
Kinetic SZE effect	$\pm 8\%$	(4)
CMB anisotropy	$\leq 1\%$	(4)
X-ray background	$\pm 2\%$	(5)
SYSTEMATIC CONTRIBUTIONS		
Presence of radio halos	$+3\%$	(4)
X-ray absolute flux calibration (S_X)	$\pm 5\%$	(6)
X-ray temperature calibration (T_e)	$\pm 7.5\%$	(7)
SZE calibration	$\pm 8\%$	(4)
(1) This paper, Section 3.3.1. (2) Sulkanen (1999). (3) La Roque et al. (2006). (4) Reese et al. (2002). (5) This paper, Section 3.3.7. (6) http://asc.harvard.edu/cal/ . (7) This paper, Section 3.3.8.		

Table 4. Results of the $r < 100$ kpc-cut isothermal β model of Section 4.2

Cluster	S_{X0} (cnt cm $^{-2}$ arcmin $^{-2}$)	r_c (arcsec)	β	ΔT_0 (mK)	kT (keV)	metallicity (Solar)	Λ (cnt cm 3 s $^{-1}$)	D_A (Gpc)
CL 0016+1609	24.2 $^{+1.0}_{-0.9}$	42.9 $^{+2.6}_{-2.4}$	0.744 $^{+0.029}_{-0.026}$	-1.36 $^{+0.08}_{-0.08}$	10.7 $^{+0.6}_{-0.7}$	0.31 $^{+0.08}_{-0.08}$	2.48 $^{+0.03}_{-0.03} \times 10^{-15}$	1.22 $^{+0.22}_{-0.19}$
Abell 0068	4.3 $^{+0.4}_{-0.3}$	59.3 $^{+7.3}_{-5.6}$	0.790 $^{+0.067}_{-0.048}$	-0.72 $^{+0.10}_{-0.11}$	9.1 $^{+1.0}_{-0.9}$	0.44 $^{+0.19}_{-0.21}$	2.98 $^{+0.09}_{-0.10} \times 10^{-15}$	0.68 $^{+0.27}_{-0.22}$
Abell 0267	6.8 $^{+1.0}_{-0.9}$	31.2 $^{+4.0}_{-3.8}$	0.656 $^{+0.029}_{-0.023}$	-0.75 $^{+0.08}_{-0.09}$	5.6 $^{+0.7}_{-0.5}$	0.24 $^{+0.19}_{-0.14}$	2.54 $^{+0.10}_{-0.08} \times 10^{-15}$	1.14 $^{+0.37}_{-0.28}$
Abell 0370	10.9 $^{+0.3}_{-0.3}$	63.6 $^{+3.3}_{-3.6}$	0.829 $^{+0.036}_{-0.037}$	-0.89 $^{+0.09}_{-0.07}$	8.6 $^{+0.5}_{-0.5}$	0.46 $^{+0.11}_{-0.11}$	2.19 $^{+0.04}_{-0.04} \times 10^{-15}$	1.83 $^{+0.41}_{-0.38}$
MS 0451.6-0305	21.5 $^{+0.9}_{-0.9}$	36.0 $^{+1.9}_{-1.6}$	0.795 $^{+0.026}_{-0.021}$	-1.45 $^{+0.08}_{-0.07}$	9.7 $^{+0.5}_{-0.6}$	0.42 $^{+0.09}_{-0.12}$	2.04 $^{+0.03}_{-0.04} \times 10^{-15}$	1.47 $^{+0.27}_{-0.23}$
MACS J0647.7+7015	25.8 $^{+3.0}_{-2.3}$	22.0 $^{+2.1}_{-2.2}$	0.654 $^{+0.029}_{-0.027}$	-1.36 $^{+0.14}_{-0.13}$	12.5 $^{+1.4}_{-1.2}$	0.18 $^{+0.11}_{-0.09}$	2.57 $^{+0.04}_{-0.04} \times 10^{-15}$	0.73 $^{+0.20}_{-0.17}$
Abell 0586	9.1 $^{+1.0}_{-0.7}$	47.3 $^{+3.9}_{-4.5}$	0.737 $^{+0.031}_{-0.033}$	-0.65 $^{+0.09}_{-0.08}$	6.3 $^{+0.4}_{-0.3}$	0.59 $^{+0.20}_{-0.14}$	2.92 $^{+0.12}_{-0.08} \times 10^{-15}$	0.74 $^{+0.17}_{-0.22}$
MACS J0744.8+3927	17.0 $^{+1.5}_{-1.4}$	26.2 $^{+2.9}_{-2.2}$	0.733 $^{+0.048}_{-0.035}$	-1.28 $^{+0.13}_{-0.15}$	8.1 $^{+0.5}_{-0.6}$	0.39 $^{+0.11}_{-0.11}$	2.35 $^{+0.06}_{-0.06} \times 10^{-15}$	1.83 $^{+0.43}_{-0.41}$
Abell 0611	31.1 $^{+4.4}_{-3.6}$	23.9 $^{+2.4}_{-2.6}$	0.618 $^{+0.017}_{-0.015}$	-0.77 $^{+0.08}_{-0.08}$	6.9 $^{+0.4}_{-0.4}$	0.39 $^{+0.11}_{-0.10}$	2.28 $^{+0.05}_{-0.04} \times 10^{-15}$	0.83 $^{+0.22}_{-0.19}$
Abell 0665	29.3 $^{+1.9}_{-1.5}$	45.2 $^{+2.7}_{-3.5}$	0.567 $^{+0.020}_{-0.018}$	-0.93 $^{+0.07}_{-0.10}$	7.7 $^{+0.4}_{-0.4}$	0.44 $^{+0.10}_{-0.08}$	3.00 $^{+0.05}_{-0.04} \times 10^{-15}$	0.76 $^{+0.16}_{-0.15}$
Abell 0697	14.0 $^{+0.6}_{-0.6}$	43.2 $^{+2.1}_{-2.2}$	0.607 $^{+0.012}_{-0.013}$	-1.22 $^{+0.12}_{-0.13}$	10.0 $^{+0.7}_{-0.6}$	0.32 $^{+0.10}_{-0.09}$	3.01 $^{+0.12}_{-0.04} \times 10^{-15}$	0.77 $^{+0.21}_{-0.17}$
Abell 0773	14.6 $^{+1.2}_{-1.1}$	37.4 $^{+3.0}_{-2.4}$	0.588 $^{+0.014}_{-0.012}$	-1.13 $^{+0.12}_{-0.10}$	7.4 $^{+0.5}_{-0.4}$	0.66 $^{+0.11}_{-0.10}$	3.18 $^{+0.06}_{-0.06} \times 10^{-15}$	1.56 $^{+0.36}_{-0.35}$
ZW 3146	85.6 $^{+2.3}_{-2.4}$	32.4 $^{+0.8}_{-0.7}$	0.745 $^{+0.007}_{-0.008}$	-1.16 $^{+0.15}_{-0.13}$	7.9 $^{+0.3}_{-0.3}$	0.27 $^{+0.05}_{-0.05}$	2.67 $^{+0.03}_{-0.02} \times 10^{-15}$	0.76 $^{+0.19}_{-0.18}$
MS 1054-0321	8.8 $^{+0.2}_{-0.2}$	70.5 $^{+6.5}_{-6.9}$	1.083 $^{+0.129}_{-0.132}$	-1.11 $^{+0.09}_{-0.09}$	9.7 $^{+1.1}_{-0.9}$	0.12 $^{+0.08}_{-0.07}$	1.80 $^{+0.03}_{-0.03} \times 10^{-15}$	1.58 $^{+0.42}_{-0.32}$
MS 1137.5+6625	17.8 $^{+3.0}_{-2.0}$	20.5 $^{+2.2}_{-2.8}$	0.833 $^{+0.057}_{-0.060}$	-0.80 $^{+0.10}_{-0.10}$	4.5 $^{+0.6}_{-0.5}$	0.79 $^{+0.44}_{-0.32}$	2.06 $^{+0.19}_{-0.15} \times 10^{-15}$	5.07 $^{+1.96}_{-1.43}$
MACS J1149.5+2223	9.5 $^{+0.4}_{-0.4}$	47.2 $^{+4.1}_{-2.7}$	0.695 $^{+0.040}_{-0.024}$	-1.14 $^{+0.13}_{-0.12}$	8.7 $^{+0.5}_{-0.5}$	0.21 $^{+0.08}_{-0.08}$	2.61 $^{+0.04}_{-0.04} \times 10^{-15}$	1.56 $^{+0.40}_{-0.32}$
Abell 1413	25.2 $^{+2.9}_{-2.5}$	36.4 $^{+3.7}_{-3.4}$	0.532 $^{+0.015}_{-0.013}$	-1.03 $^{+0.14}_{-0.14}$	7.5 $^{+0.4}_{-0.3}$	0.37 $^{+0.06}_{-0.06}$	3.05 $^{+0.03}_{-0.03} \times 10^{-15}$	0.62 $^{+0.19}_{-0.16}$
CL J1226.9+3332	21.9 $^{+4.4}_{-4.1}$	16.4 $^{+3.9}_{-2.1}$	0.734 $^{+0.082}_{-0.042}$	-1.69 $^{+0.19}_{-0.16}$	14.0 $^{+2.1}_{-1.8}$	0.17 $^{+0.13}_{-0.10}$	2.45 $^{+0.05}_{-0.05} \times 10^{-15}$	0.81 $^{+0.28}_{-0.22}$
MACS J1311.0-0310	65.5 $^{+35.8}_{-35.3}$	7.43 $^{+3.2}_{-1.2}$	0.633 $^{+0.029}_{-0.022}$	-1.53 $^{+0.26}_{-0.25}$	6.8 $^{+1.4}_{-1.0}$	0.38 $^{+0.16}_{-0.19}$	2.67 $^{+0.11}_{-0.14} \times 10^{-15}$	1.50 $^{+0.76}_{-0.50}$
Abell 1689	36.1 $^{+1.4}_{-1.3}$	48.0 $^{+1.5}_{-1.7}$	0.686 $^{+0.010}_{-0.010}$	-1.66 $^{+0.13}_{-0.14}$	10.1 $^{+0.5}_{-0.6}$	0.29 $^{+0.08}_{-0.10}$	2.96 $^{+0.03}_{-0.04} \times 10^{-15}$	0.90 $^{+0.16}_{-0.19}$
RX J1347.5-1145	236.2 $^{+11.7}_{-13.4}$	17.2 $^{+0.6}_{-0.6}$	0.633 $^{+0.005}_{-0.005}$	-2.75 $^{+0.28}_{-0.30}$	16.1 $^{+1.0}_{-0.9}$	0.32 $^{+0.08}_{-0.09}$	2.79 $^{+0.03}_{-0.03} \times 10^{-15}$	0.51 $^{+0.12}_{-0.11}$
MS 1358.4+6245	18.7 $^{+1.0}_{-0.9}$	31.9 $^{+1.2}_{-1.5}$	0.658 $^{+0.010}_{-0.012}$	-0.69 $^{+0.10}_{-0.10}$	8.5 $^{+0.7}_{-0.6}$	0.54 $^{+0.16}_{-0.13}$	2.39 $^{+0.06}_{-0.05} \times 10^{-15}$	0.81 $^{+0.28}_{-0.23}$
Abell 1835	62.8 $^{+3.0}_{-2.7}$	32.4 $^{+1.4}_{-1.1}$	0.670 $^{+0.012}_{-0.009}$	-1.70 $^{+0.10}_{-0.11}$	10.9 $^{+0.7}_{-0.5}$	0.38 $^{+0.09}_{-0.08}$	2.35 $^{+0.03}_{-0.03} \times 10^{-15}$	0.69 $^{+0.16}_{-0.09}$
MACS J1423+2404	156.5 $^{+19.2}_{-18.2}$	11.2 $^{+0.9}_{-0.7}$	0.607 $^{+0.011}_{-0.009}$	-1.39 $^{+0.24}_{-0.21}$	7.4 $^{+0.4}_{-0.4}$	0.36 $^{+0.08}_{-0.08}$	2.19 $^{+0.03}_{-0.04} \times 10^{-15}$	1.71 $^{+0.65}_{-0.57}$
Abell 1914	78.7 $^{+2.4}_{-2.7}$	45.3 $^{+1.5}_{-2.1}$	0.742 $^{+0.011}_{-0.008}$	-1.55 $^{+0.15}_{-0.13}$	9.6 $^{+0.3}_{-0.3}$	0.24 $^{+0.05}_{-0.06}$	3.10 $^{+0.03}_{-0.03} \times 10^{-15}$	0.67 $^{+0.12}_{-0.13}$
Abell 1995	24.9 $^{+0.4}_{-0.4}$	50.4 $^{+1.4}_{-1.5}$	0.923 $^{+0.021}_{-0.023}$	-0.92 $^{+0.05}_{-0.05}$	9.1 $^{+0.5}_{-0.5}$	0.45 $^{+0.13}_{-0.11}$	2.35 $^{+0.05}_{-0.04} \times 10^{-15}$	1.20 $^{+0.21}_{-0.16}$
Abell 2111	2.3 $^{+0.2}_{-0.2}$	58.8 $^{+7.1}_{-6.6}$	0.648 $^{+0.043}_{-0.038}$	-0.57 $^{+0.11}_{-0.11}$	8.2 $^{+0.8}_{-0.8}$	0.19 $^{+0.13}_{-0.12}$	2.76 $^{+0.06}_{-0.05} \times 10^{-15}$	0.72 $^{+0.35}_{-0.28}$
Abell 2163 ^a	69.2 $^{+0.7}_{-0.7}$	78.8 $^{+0.6}_{-0.6}$	0.700 $^{+0.011}_{-0.011}$	-1.55 $^{+0.15}_{-0.15}$	13.8 $^{+0.8}_{-0.7}$	0.23 $^{+0.04}_{-0.04}$	2.52 $^{+0.01}_{-0.01} \times 10^{-15}$	0.73 $^{+0.27}_{-0.22}$
Abell 2204	27.0 $^{+8.0}_{-4.9}$	35.9 $^{+8.4}_{-7.4}$	0.623 $^{+0.066}_{-0.049}$	-1.62 $^{+0.21}_{-0.27}$	11.2 $^{+0.7}_{-0.7}$	0.46 $^{+0.15}_{-0.12}$	2.36 $^{+0.05}_{-0.04} \times 10^{-15}$	0.46 $^{+0.11}_{-0.10}$
Abell 2218	20.9 $^{+0.3}_{-0.3}$	70.4 $^{+7.4}_{-6.6}$	0.767 $^{+0.015}_{-0.012}$	-0.87 $^{+0.07}_{-0.07}$	7.8 $^{+0.4}_{-0.4}$	0.35 $^{+0.08}_{-0.08}$	3.01 $^{+0.04}_{-0.04} \times 10^{-15}$	1.18 $^{+0.24}_{-0.22}$
RX J1716.4+6708	11.0 $^{+3.3}_{-1.8}$	14.7 $^{+3.5}_{-3.5}$	0.624 $^{+0.070}_{-0.070}$	-0.70 $^{+0.15}_{-0.19}$	5.8 $^{+0.7}_{-0.7}$	0.87 $^{+0.35}_{-0.30}$	2.18 $^{+0.16}_{-0.11} \times 10^{-15}$	2.09 $^{+1.07}_{-0.80}$
Abell 2259	5.4 $^{+0.5}_{-0.3}$	48.1 $^{+3.6}_{-4.5}$	0.611 $^{+0.022}_{-0.026}$	-0.45 $^{+0.14}_{-0.14}$	5.7 $^{+0.5}_{-0.4}$	0.35 $^{+0.12}_{-0.12}$	3.01 $^{+0.09}_{-0.08} \times 10^{-15}$	0.51 $^{+0.37}_{-0.29}$
Abell 2261	14.4 $^{+2.2}_{-2.3}$	29.2 $^{+4.8}_{-2.9}$	0.628 $^{+0.030}_{-0.020}$	-1.18 $^{+0.12}_{-0.12}$	7.9 $^{+0.8}_{-1.1}$	0.55 $^{+0.42}_{-0.29}$	2.80 $^{+0.21}_{-0.12} \times 10^{-15}$	0.95 $^{+0.30}_{-0.26}$
MS 2053.7-0449	9.4 $^{+1.6}_{-1.1}$	24.4 $^{+3.1}_{-3.2}$	0.775 $^{+0.050}_{-0.055}$	-0.44 $^{+0.07}_{-0.08}$	4.5 $^{+0.6}_{-0.5}$	0.46 $^{+0.24}_{-0.22}$	2.14 $^{+0.12}_{-0.12} \times 10^{-15}$	3.58 $^{+1.62}_{-1.24}$
MACS J2129.4-0741	41.1 $^{+10.6}_{-7.2}$	14.2 $^{+2.9}_{-2.9}$	0.605 $^{+0.020}_{-0.018}$	-1.40 $^{+0.19}_{-0.15}$	8.3 $^{+0.8}_{-0.7}$	0.65 $^{+0.18}_{-0.14}$	2.70 $^{+0.08}_{-0.06} \times 10^{-15}$	1.22 $^{+0.34}_{-0.28}$
RX J2129.7+0005	13.3 $^{+2.3}_{-1.9}$	26.9 $^{+2.9}_{-3.2}$	0.617 $^{+0.017}_{-0.017}$	-0.75 $^{+0.10}_{-0.11}$	6.9 $^{+0.7}_{-0.7}$	0.46 $^{+0.23}_{-0.18}$	2.83 $^{+0.13}_{-0.10} \times 10^{-15}$	0.56 $^{+0.21}_{-0.16}$

Table 4—Continued

Cluster	S_{X0} (cnt cm $^{-2}$ arcmin $^{-2}$)	r_c (arcsec)	β	ΔT_0 (mK)	kT (keV)	metallicity (Solar)	Λ (cnt cm 3 s $^{-1}$)	D_A (Gpc)
MACS J2214.9-1359	$19.3^{+2.2}_{-1.9}$	$30.5^{+3.1}_{-3.3}$	$0.700^{+0.038}_{-0.038}$	$-1.45^{+0.12}_{-0.13}$	$9.9^{+1.1}_{-0.7}$	$0.29^{+0.13}_{-0.13}$	$2.84^{+0.06}_{-0.06} \times 10^{-15}$	$1.86^{+0.42}_{-0.34}$
MACS J2228.5+2036	$18.2^{+3.5}_{-2.8}$	$17.8^{+3.1}_{-2.6}$	$0.532^{+0.024}_{-0.022}$	$-1.75^{+0.21}_{-0.19}$	$8.4^{+0.8}_{-0.8}$	$0.35^{+0.13}_{-0.10}$	$2.73^{+0.07}_{-0.05} \times 10^{-15}$	$1.99^{+0.47}_{-0.44}$

^aNOTE: The disturbed morphology of Abell 2163 (see Appendix A1) required us to fix the value of the β parameter to a fiducial value of 0.7.

Table 5. Results of the isothermal β model of Section 4.2

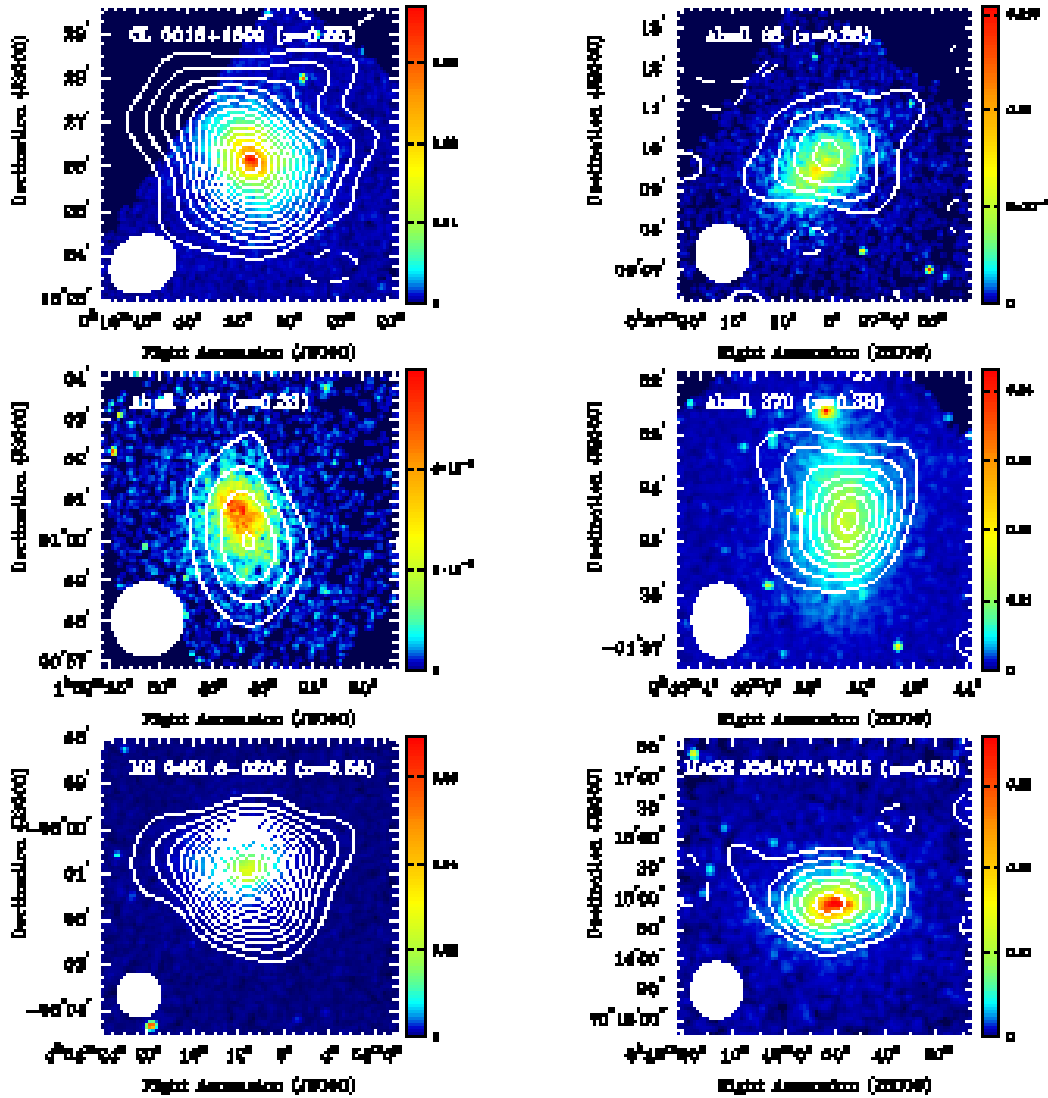
Cluster	S_{X0} (cnt cm $^{-2}$ arcmin $^{-2}$)	r_c (arcsec)	β	ΔT_0 (mK)	kT (keV)	metallicity (Solar)	Λ (cnt cm 3 s $^{-1}$)	D_A (Gpc)
CL 0016+1609	27.4 $^{+0.7}_{-0.6}$	36.7 $^{+1.4}_{-1.5}$	0.686 $^{+0.017}_{-0.017}$	-1.44 $^{+0.09}_{-0.09}$	10.3 $^{+0.5}_{-0.5}$	0.37 $^{+0.07}_{-0.07}$	2.50 $^{+0.03}_{-0.03} \times 10^{-15}$	1.30 $^{+0.21}_{-0.19}$
Abell 0068	5.0 $^{+0.2}_{-0.2}$	49.6 $^{+3.6}_{-3.1}$	0.721 $^{+0.035}_{-0.029}$	-0.75 $^{+0.10}_{-0.11}$	10.0 $^{+1.1}_{-0.9}$	0.42 $^{+0.19}_{-0.18}$	2.98 $^{+0.08}_{-0.08} \times 10^{-15}$	0.54 $^{+0.20}_{-0.16}$
Abell 0267	4.6 $^{+0.2}_{-0.2}$	41.3 $^{+2.8}_{-2.6}$	0.712 $^{+0.030}_{-0.029}$	-0.70 $^{+0.08}_{-0.07}$	6.0 $^{+0.6}_{-0.5}$	0.24 $^{+0.17}_{-0.13}$	2.57 $^{+0.09}_{-0.07} \times 10^{-15}$	1.13 $^{+0.34}_{-0.27}$
Abell 0370	11.7 $^{+0.2}_{-0.2}$	57.0 $^{+2.5}_{-2.6}$	0.768 $^{+0.029}_{-0.027}$	-0.89 $^{+0.09}_{-0.10}$	8.9 $^{+0.4}_{-0.4}$	0.47 $^{+0.09}_{-0.09}$	2.20 $^{+0.03}_{-0.03} \times 10^{-15}$	1.64 $^{+0.40}_{-0.34}$
MS 0451.6-0305	23.3 $^{+0.5}_{-0.5}$	33.5 $^{+1.2}_{-1.2}$	0.767 $^{+0.018}_{-0.018}$	-1.48 $^{+0.09}_{-0.09}$	10.4 $^{+0.6}_{-0.7}$	0.45 $^{+0.10}_{-0.10}$	2.06 $^{+0.03}_{-0.03} \times 10^{-15}$	1.26 $^{+0.22}_{-0.19}$
MACS J0647.7+7015	31.0 $^{+1.1}_{-1.1}$	19.7 $^{+0.8}_{-0.8}$	0.645 $^{+0.012}_{-0.012}$	-1.39 $^{+0.12}_{-0.12}$	13.8 $^{+1.6}_{-1.3}$	0.25 $^{+0.14}_{-0.12}$	2.61 $^{+0.05}_{-0.05} \times 10^{-15}$	0.59 $^{+0.17}_{-0.14}$
Abell 0586	13.7 $^{+0.5}_{-0.5}$	32.6 $^{+1.6}_{-1.5}$	0.639 $^{+0.015}_{-0.014}$	-0.72 $^{+0.09}_{-0.09}$	6.6 $^{+0.4}_{-0.4}$	0.54 $^{+0.12}_{-0.12}$	2.90 $^{+0.07}_{-0.07} \times 10^{-15}$	0.61 $^{+0.18}_{-0.15}$
MACS J0744.8+3927	86.4 $^{+6.2}_{-5.9}$	6.7 $^{+0.5}_{-0.4}$	0.516 $^{+0.008}_{-0.007}$	-2.17 $^{+0.23}_{-0.23}$	8.2 $^{+0.6}_{-0.6}$	0.19 $^{+0.09}_{-0.09}$	2.28 $^{+0.04}_{-0.04} \times 10^{-15}$	1.64 $^{+0.41}_{-0.36}$
Abell 0611	39.9 $^{+1.2}_{-1.1}$	19.9 $^{+0.7}_{-0.7}$	0.592 $^{+0.008}_{-0.007}$	-0.80 $^{+0.09}_{-0.09}$	6.8 $^{+0.3}_{-0.3}$	0.39 $^{+0.08}_{-0.08}$	2.28 $^{+0.03}_{-0.03} \times 10^{-15}$	0.76 $^{+0.18}_{-0.17}$
Abell 0665	23.1 $^{+0.4}_{-0.4}$	49.4 $^{+1.5}_{-1.5}$	0.536 $^{+0.008}_{-0.008}$	-1.04 $^{+0.10}_{-0.10}$	7.3 $^{+0.2}_{-0.2}$	0.35 $^{+0.06}_{-0.06}$	2.95 $^{+0.03}_{-0.03} \times 10^{-15}$	1.01 $^{+0.22}_{-0.18}$
Abell 0697	14.2 $^{+0.4}_{-0.4}$	42.9 $^{+1.8}_{-1.5}$	0.607 $^{+0.011}_{-0.010}$	-1.22 $^{+0.12}_{-0.12}$	9.9 $^{+0.6}_{-0.6}$	0.41 $^{+0.09}_{-0.09}$	3.05 $^{+0.04}_{-0.04} \times 10^{-15}$	0.77 $^{+0.20}_{-0.17}$
Abell 0773	12.4 $^{+0.3}_{-0.3}$	43.3 $^{+1.4}_{-1.4}$	0.613 $^{+0.010}_{-0.010}$	-1.08 $^{+0.11}_{-0.11}$	7.6 $^{+0.5}_{-0.4}$	0.60 $^{+0.09}_{-0.09}$	3.14 $^{+0.06}_{-0.05} \times 10^{-15}$	1.51 $^{+0.37}_{-0.32}$
ZW 3146	571.5 $^{+9.6}_{-9.5}$	9.0 $^{+0.1}_{-0.1}$	0.567 $^{+0.002}_{-0.002}$	-2.02 $^{+0.25}_{-0.25}$	6.6 $^{+0.1}_{-0.1}$	0.38 $^{+0.03}_{-0.03}$	2.67 $^{+0.02}_{-0.02} \times 10^{-15}$	0.98 $^{+0.26}_{-0.23}$
MS 1054-0321	8.9 $^{+0.2}_{-0.2}$	68.7 $^{+10.6}_{-8.4}$	1.045 $^{+0.213}_{-0.146}$	-1.12 $^{+0.09}_{-0.11}$	9.8 $^{+1.1}_{-1.1}$	0.12 $^{+0.10}_{-0.07}$	1.81 $^{+0.03}_{-0.04} \times 10^{-15}$	1.60 $^{+0.43}_{-0.37}$
MS 1137.5+6625	24.8 $^{+1.4}_{-1.4}$	15.5 $^{+1.2}_{-1.2}$	0.739 $^{+0.034}_{-0.031}$	-0.90 $^{+0.10}_{-0.10}$	5.3 $^{+0.5}_{-0.5}$	0.54 $^{+0.26}_{-0.22}$	2.04 $^{+0.10}_{-0.09} \times 10^{-15}$	3.65 $^{+1.25}_{-0.97}$
MACS J1149.5+2223	10.9 $^{+0.4}_{-0.3}$	39.4 $^{+1.7}_{-1.7}$	0.633 $^{+0.015}_{-0.014}$	-1.21 $^{+0.12}_{-0.12}$	9.8 $^{+0.7}_{-0.7}$	0.24 $^{+0.10}_{-0.09}$	2.66 $^{+0.05}_{-0.04} \times 10^{-15}$	1.26 $^{+0.31}_{-0.27}$
Abell 1413	44.8 $^{+1.1}_{-1.1}$	21.1 $^{+0.7}_{-0.6}$	0.476 $^{+0.004}_{-0.004}$	-1.24 $^{+0.18}_{-0.18}$	7.3 $^{+0.2}_{-0.2}$	0.46 $^{+0.07}_{-0.06}$	3.09 $^{+0.03}_{-0.03} \times 10^{-15}$	0.62 $^{+0.20}_{-0.16}$
CL J1226.9+3332	22.9 $^{+1.5}_{-1.4}$	15.3 $^{+1.4}_{-1.3}$	0.701 $^{+0.041}_{-0.036}$	-1.73 $^{+0.17}_{-0.17}$	12.7 $^{+2.0}_{-1.6}$	0.21 $^{+0.18}_{-0.12}$	2.44 $^{+0.07}_{-0.05} \times 10^{-15}$	0.98 $^{+0.35}_{-0.27}$
MACS J1311.0-0310	33.7 $^{+2.4}_{-2.2}$	9.5 $^{+0.7}_{-0.7}$	0.624 $^{+0.020}_{-0.019}$	-1.33 $^{+0.20}_{-0.21}$	6.4 $^{+0.6}_{-0.5}$	0.54 $^{+0.18}_{-0.19}$	2.72 $^{+0.10}_{-0.11} \times 10^{-15}$	1.97 $^{+0.75}_{-0.60}$
Abell 1689	102.4 $^{+1.7}_{-1.8}$	20.7 $^{+0.4}_{-0.4}$	0.554 $^{+0.003}_{-0.003}$	-2.06 $^{+0.17}_{-0.16}$	10.0 $^{+0.3}_{-0.3}$	0.37 $^{+0.05}_{-0.05}$	3.00 $^{+0.02}_{-0.02} \times 10^{-15}$	0.70 $^{+0.13}_{-0.11}$
RX J1347.5-1145	1837.0 $^{+30.0}_{-30.0}$	4.8 $^{+0.1}_{-0.1}$	0.542 $^{+0.001}_{-0.001}$	-5.15 $^{+0.58}_{-0.60}$	13.5 $^{+0.5}_{-0.5}$	0.37 $^{+0.05}_{-0.05}$	2.80 $^{+0.02}_{-0.02} \times 10^{-15}$	0.76 $^{+0.20}_{-0.17}$
MS 1358.4+6245	113.1 $^{+5.0}_{-4.5}$	6.6 $^{+0.3}_{-0.3}$	0.483 $^{+0.003}_{-0.003}$	-1.36 $^{+0.18}_{-0.18}$	8.3 $^{+0.6}_{-0.6}$	0.76 $^{+0.17}_{-0.16}$	2.48 $^{+0.07}_{-0.07} \times 10^{-15}$	1.11 $^{+0.38}_{-0.30}$
Abell 1835	524.9 $^{+7.1}_{-7.4}$	8.1 $^{+0.1}_{-0.1}$	0.543 $^{+0.001}_{-0.001}$	-2.90 $^{+0.21}_{-0.20}$	8.4 $^{+0.2}_{-0.2}$	0.42 $^{+0.05}_{-0.05}$	2.36 $^{+0.02}_{-0.02} \times 10^{-15}$	0.98 $^{+0.16}_{-0.14}$
MACS J1423.8+2504	1219.0 $^{+12.2}_{-14.4}$	3.59 $^{+0.01}_{-0.01}$	0.550 $^{+0.001}_{-0.001}$	-2.41 $^{+0.41}_{-0.41}$	5.8 $^{+0.2}_{-0.2}$	0.56 $^{+0.05}_{-0.05}$	2.19 $^{+0.02}_{-0.02} \times 10^{-15}$	2.52 $^{+0.86}_{-0.77}$
Abell 1914	48.2 $^{+0.5}_{-0.5}$	68.8 $^{+1.1}_{-1.6}$	0.903 $^{+0.013}_{-0.012}$	-1.36 $^{+0.11}_{-0.12}$	9.9 $^{+0.3}_{-0.3}$	0.25 $^{+0.05}_{-0.05}$	3.11 $^{+0.02}_{-0.02} \times 10^{-15}$	0.68 $^{+0.13}_{-0.12}$
Abell 1995	25.0 $^{+0.4}_{-0.4}$	50.1 $^{+1.6}_{-1.5}$	0.918 $^{+0.024}_{-0.023}$	-0.90 $^{+0.05}_{-0.06}$	8.7 $^{+0.4}_{-0.4}$	0.46 $^{+0.09}_{-0.09}$	2.35 $^{+0.03}_{-0.03} \times 10^{-15}$	1.30 $^{+0.21}_{-0.18}$
Abell 2111	2.6 $^{+0.1}_{-0.1}$	51.4 $^{+4.5}_{-4.2}$	0.613 $^{+0.031}_{-0.028}$	-0.59 $^{+0.12}_{-0.12}$	8.1 $^{+0.9}_{-0.8}$	0.14 $^{+0.12}_{-0.12}$	2.74 $^{+0.05}_{-0.04} \times 10^{-15}$	0.72 $^{+0.36}_{-0.28}$
Abell 2163	64.6 $^{+0.5}_{-0.5}$	68.8 $^{+1.1}_{-1.0}$	0.576 $^{+0.006}_{-0.005}$	-1.89 $^{+0.17}_{-0.17}$	14.8 $^{+0.4}_{-0.3}$	0.34 $^{+0.04}_{-0.04}$	2.56 $^{+0.01}_{-0.01} \times 10^{-15}$	0.42 $^{+0.08}_{-0.07}$
Abell 2204	428.3 $^{+9.1}_{-8.9}$	5.2 $^{+0.1}_{-0.1}$	0.483 $^{+0.002}_{-0.002}$	-3.22 $^{+0.30}_{-0.32}$	6.5 $^{+0.2}_{-0.2}$	0.64 $^{+0.06}_{-0.06}$	2.44 $^{+0.02}_{-0.02} \times 10^{-15}$	1.08 $^{+0.23}_{-0.20}$
Abell 2218	20.8 $^{+0.3}_{-0.3}$	70.4 $^{+1.7}_{-1.6}$	0.766 $^{+0.014}_{-0.012}$	-0.87 $^{+0.08}_{-0.08}$	8.2 $^{+0.4}_{-0.4}$	0.33 $^{+0.07}_{-0.07}$	3.01 $^{+0.03}_{-0.03} \times 10^{-15}$	1.07 $^{+0.22}_{-0.20}$
RX J1716.4+6708	11.4 $^{+1.3}_{-1.0}$	12.4 $^{+1.8}_{-1.8}$	0.577 $^{+0.033}_{-0.033}$	-0.76 $^{+0.17}_{-0.17}$	7.7 $^{+1.2}_{-1.0}$	0.66 $^{+0.25}_{-0.25}$	2.24 $^{+0.11}_{-0.11} \times 10^{-15}$	1.31 $^{+0.53}_{-0.53}$
Abell 2259	5.9 $^{+0.2}_{-0.2}$	42.4 $^{+3.1}_{-2.6}$	0.579 $^{+0.021}_{-0.018}$	-0.46 $^{+0.16}_{-0.16}$	5.6 $^{+0.3}_{-0.3}$	0.49 $^{+0.12}_{-0.11}$	3.09 $^{+0.08}_{-0.08} \times 10^{-15}$	0.52 $^{+0.43}_{-0.30}$
Abell 2261	25.1 $^{+0.9}_{-0.9}$	18.4 $^{+0.8}_{-0.7}$	0.559 $^{+0.008}_{-0.008}$	-1.36 $^{+0.13}_{-0.14}$	7.2 $^{+0.4}_{-0.4}$	0.44 $^{+0.13}_{-0.12}$	2.74 $^{+0.06}_{-0.05} \times 10^{-15}$	0.99 $^{+0.25}_{-0.22}$
MS 2053.7-0449	15.0 $^{+1.2}_{-1.0}$	15.3 $^{+1.6}_{-1.4}$	0.639 $^{+0.033}_{-0.029}$	-0.52 $^{+0.09}_{-0.09}$	4.7 $^{+0.5}_{-0.4}$	0.28 $^{+0.16}_{-0.14}$	2.07 $^{+0.09}_{-0.09} \times 10^{-15}$	3.11 $^{+1.27}_{-0.99}$
MACS J2129.4-0741	21.9 $^{+1.0}_{-0.9}$	22.0 $^{+1.3}_{-1.3}$	0.678 $^{+0.023}_{-0.021}$	-1.22 $^{+0.13}_{-0.14}$	8.6 $^{+0.7}_{-0.6}$	0.69 $^{+0.13}_{-0.13}$	2.72 $^{+0.06}_{-0.06} \times 10^{-15}$	1.39 $^{+0.39}_{-0.33}$
RX J2129.7+0005	66.5 $^{+3.6}_{-3.5}$	8.0 $^{+0.4}_{-0.4}$	0.507 $^{+0.005}_{-0.005}$	-1.21 $^{+0.19}_{-0.19}$	5.9 $^{+0.3}_{-0.3}$	0.53 $^{+0.09}_{-0.10}$	2.82 $^{+0.05}_{-0.06} \times 10^{-15}$	0.76 $^{+0.27}_{-0.21}$

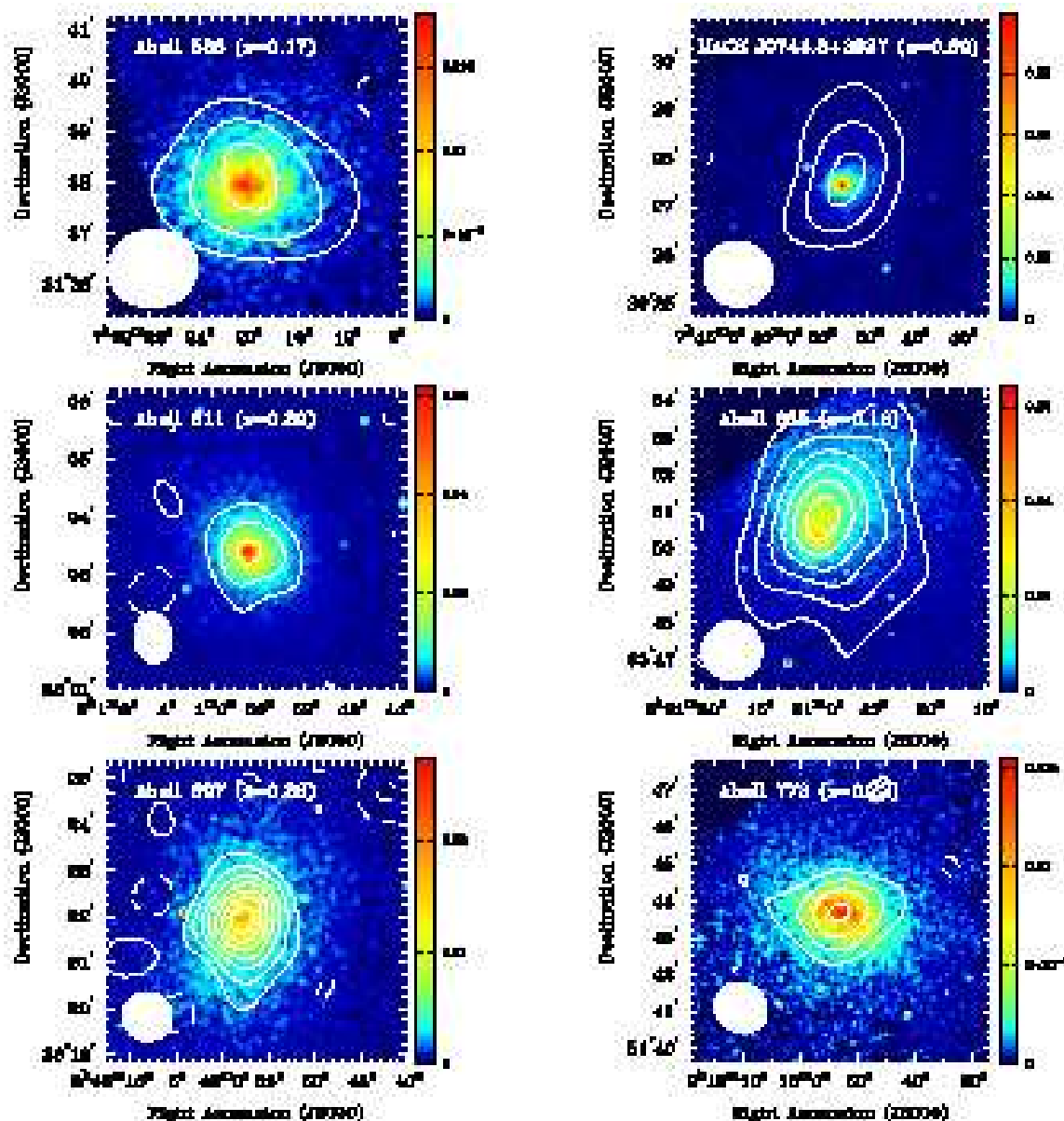
Table 5—Continued

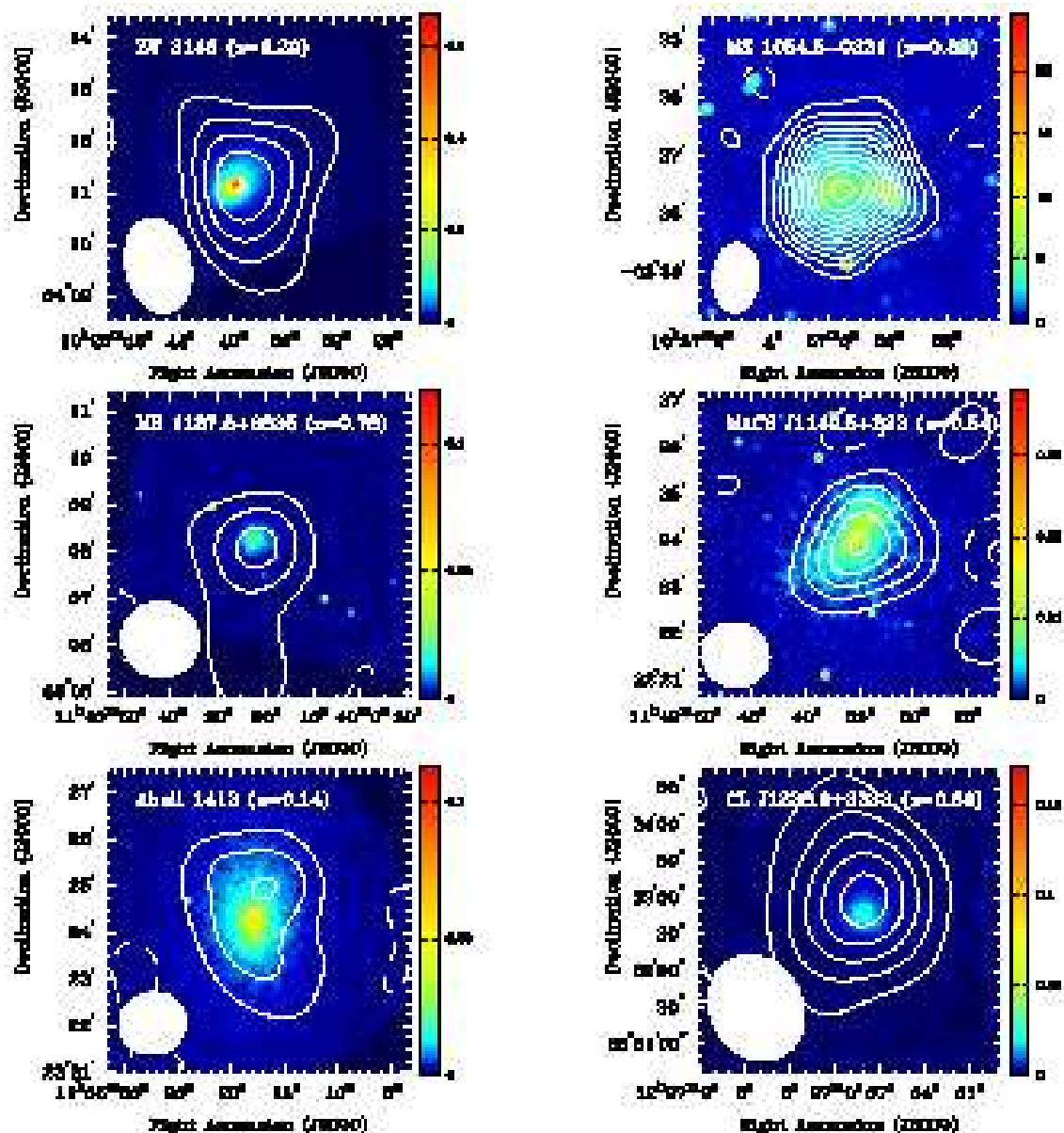
Cluster	S_{X0} (cnt cm $^{-2}$ arcmin $^{-2}$)	r_c (arcsec)	β	ΔT_0 (mK)	kT (keV)	metallicity (Solar)	Λ (cnt cm 3 s $^{-1}$)	D_A (Gpc)
MACS J2214.9-1359	$24.9^{+1.0}_{-0.9}$	$22.7^{+1.3}_{-1.2}$	$0.618^{+0.017}_{-0.016}$	$-1.65^{+0.13}_{-0.14}$	$9.8^{+0.8}_{-0.7}$	$0.25^{+0.10}_{-0.10}$	$2.82^{+0.05}_{-0.05} \times 10^{-15}$	$1.97^{+0.43}_{-0.38}$
MACS J2228.5+2036	$12.5^{+0.6}_{-0.6}$	$22.4^{+1.3}_{-1.3}$	$0.532^{+0.011}_{-0.011}$	$-1.68^{+0.16}_{-0.16}$	$9.1^{+0.8}_{-0.7}$	$0.41^{+0.12}_{-0.13}$	$2.78^{+0.05}_{-0.06} \times 10^{-15}$	$1.85^{+0.47}_{-0.39}$

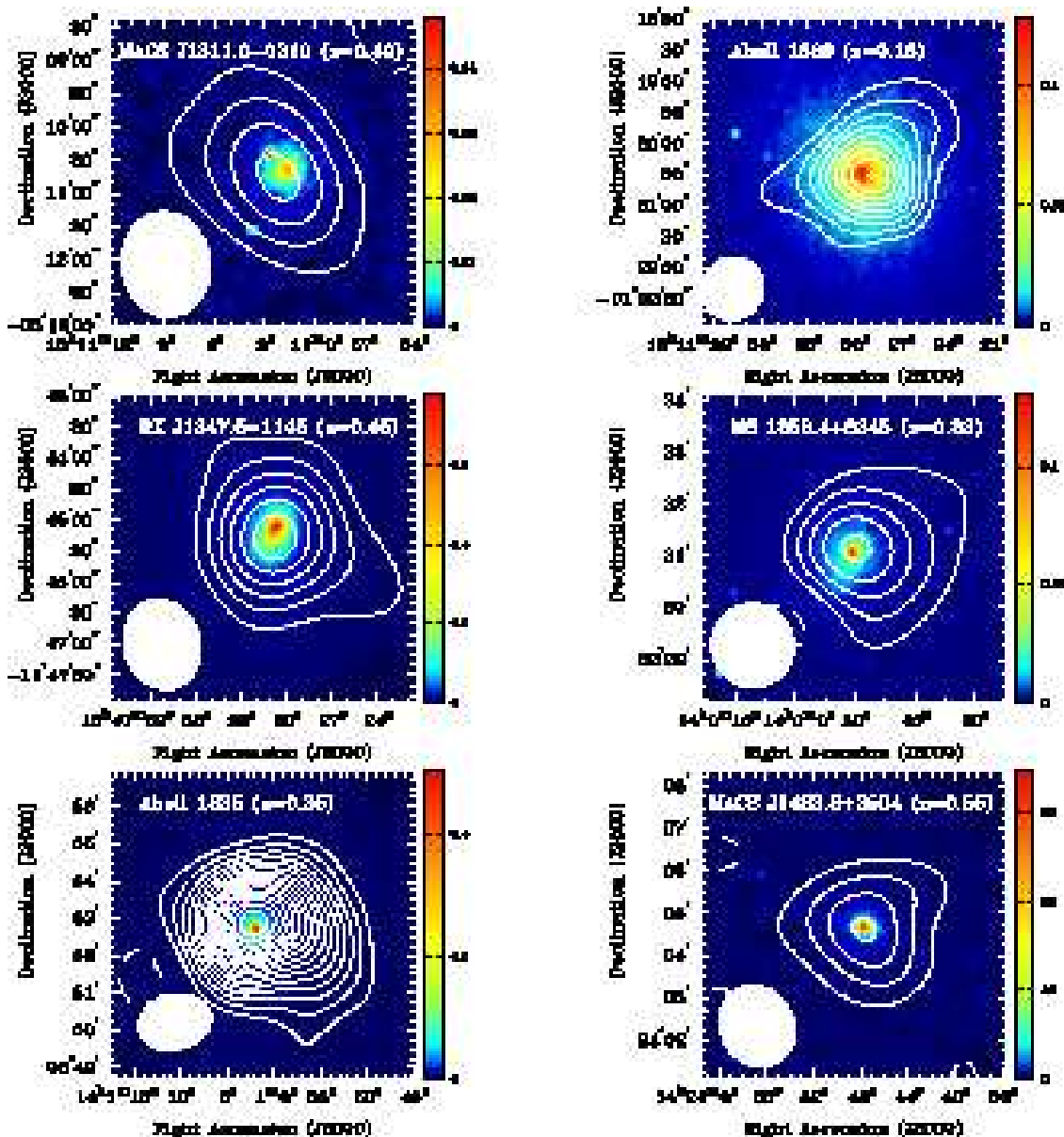
Appendix 1: X-ray and SZE images

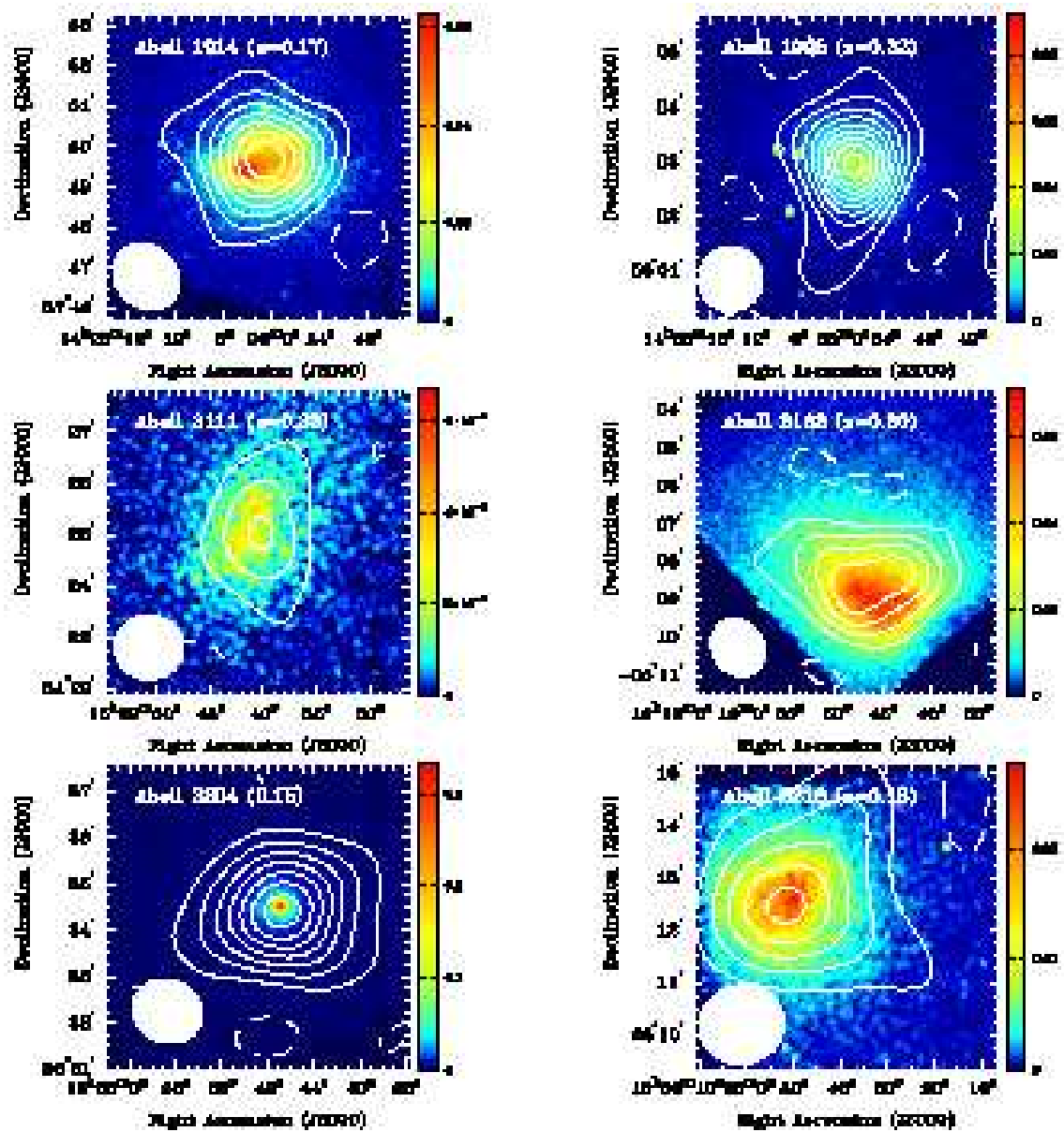
Fig. 5.— *Chandra* images of the background-subtracted X-ray surface brightness in 0.7-7 keV band (color) in units of counts pixel⁻¹ (1.97" pixels). Overlaid are the SZE decrement contours, with contour levels (+1,-1,-2,-3,-4,...) times the rms noise in each image. The full-width at half maximum of the synthesized beams (effective psf) of these deconvolutions are shown in the lower left-hand corners.

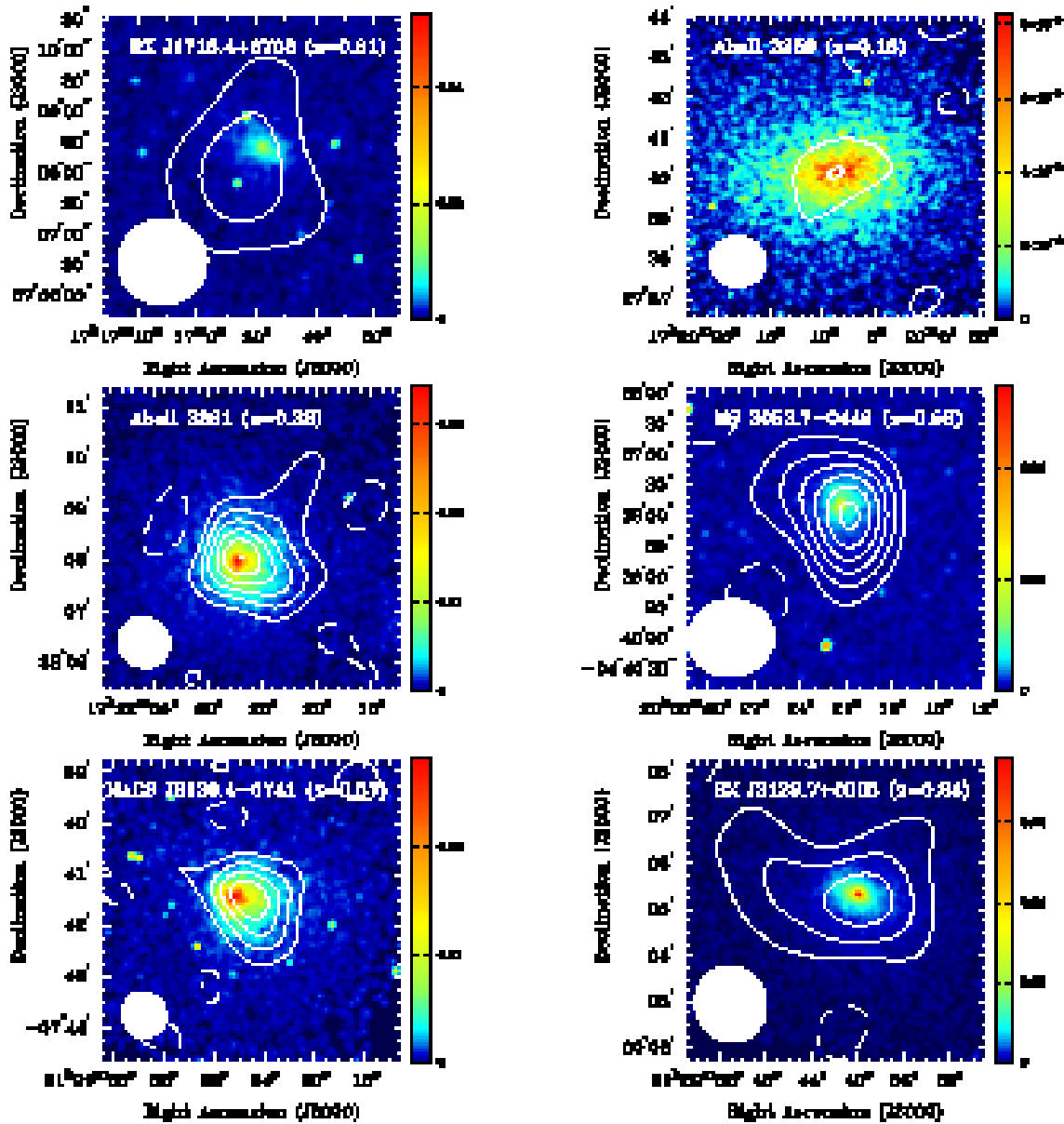


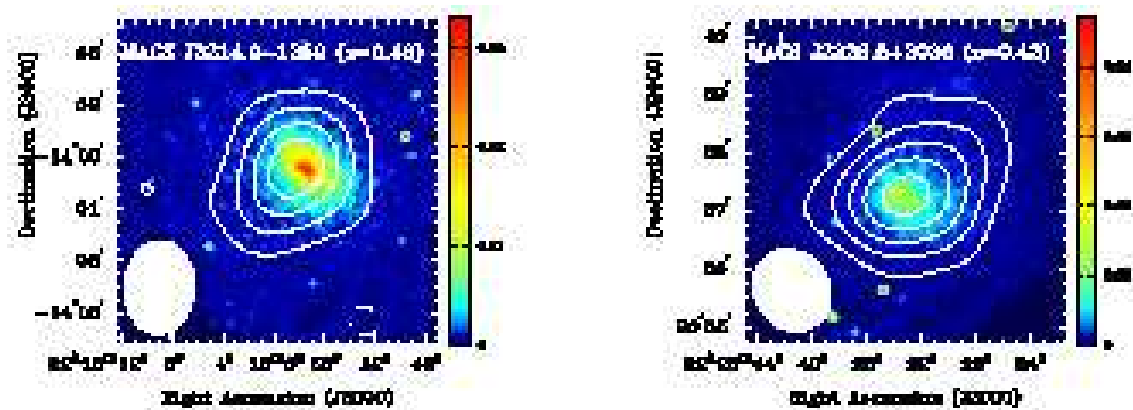








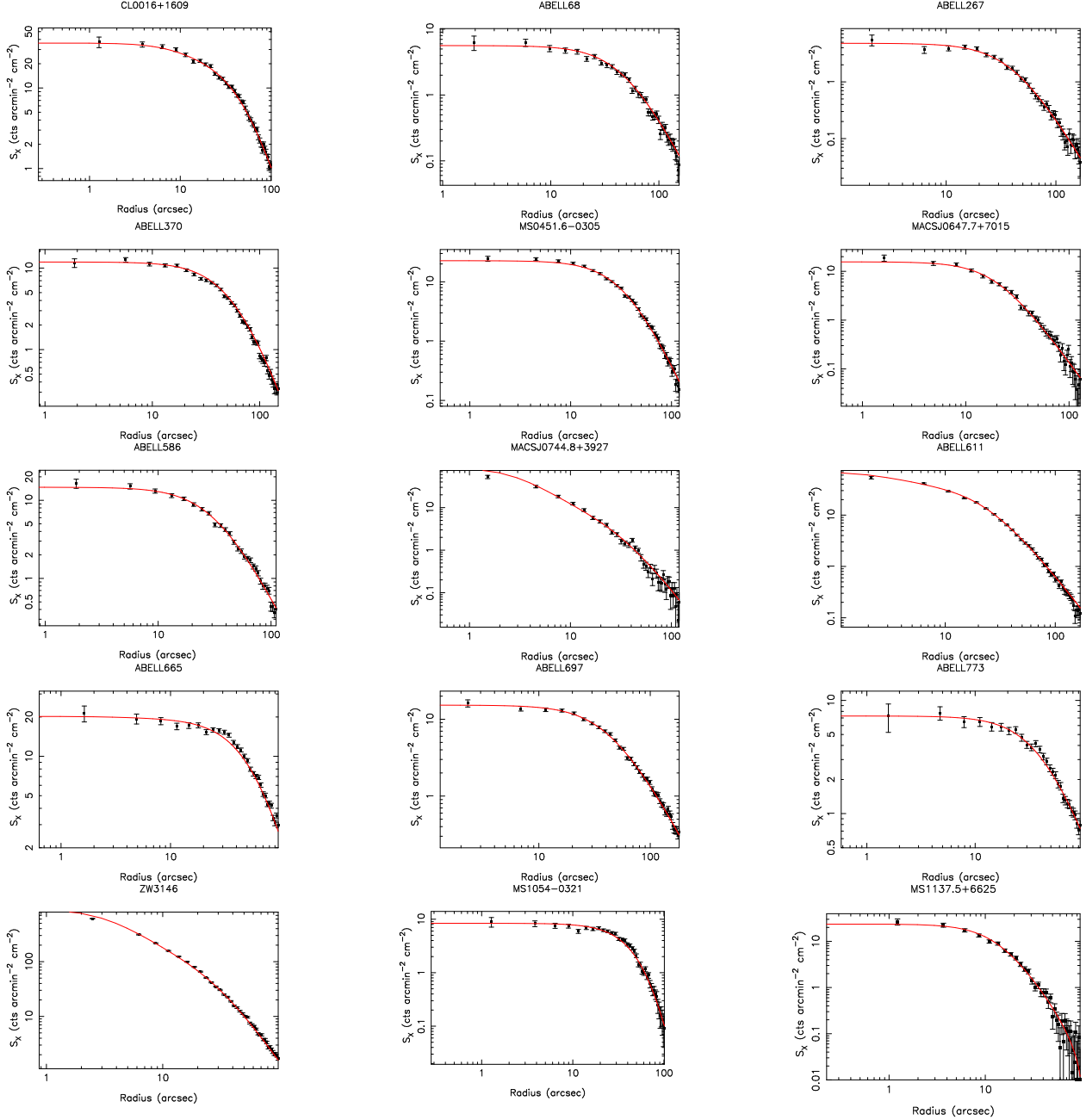


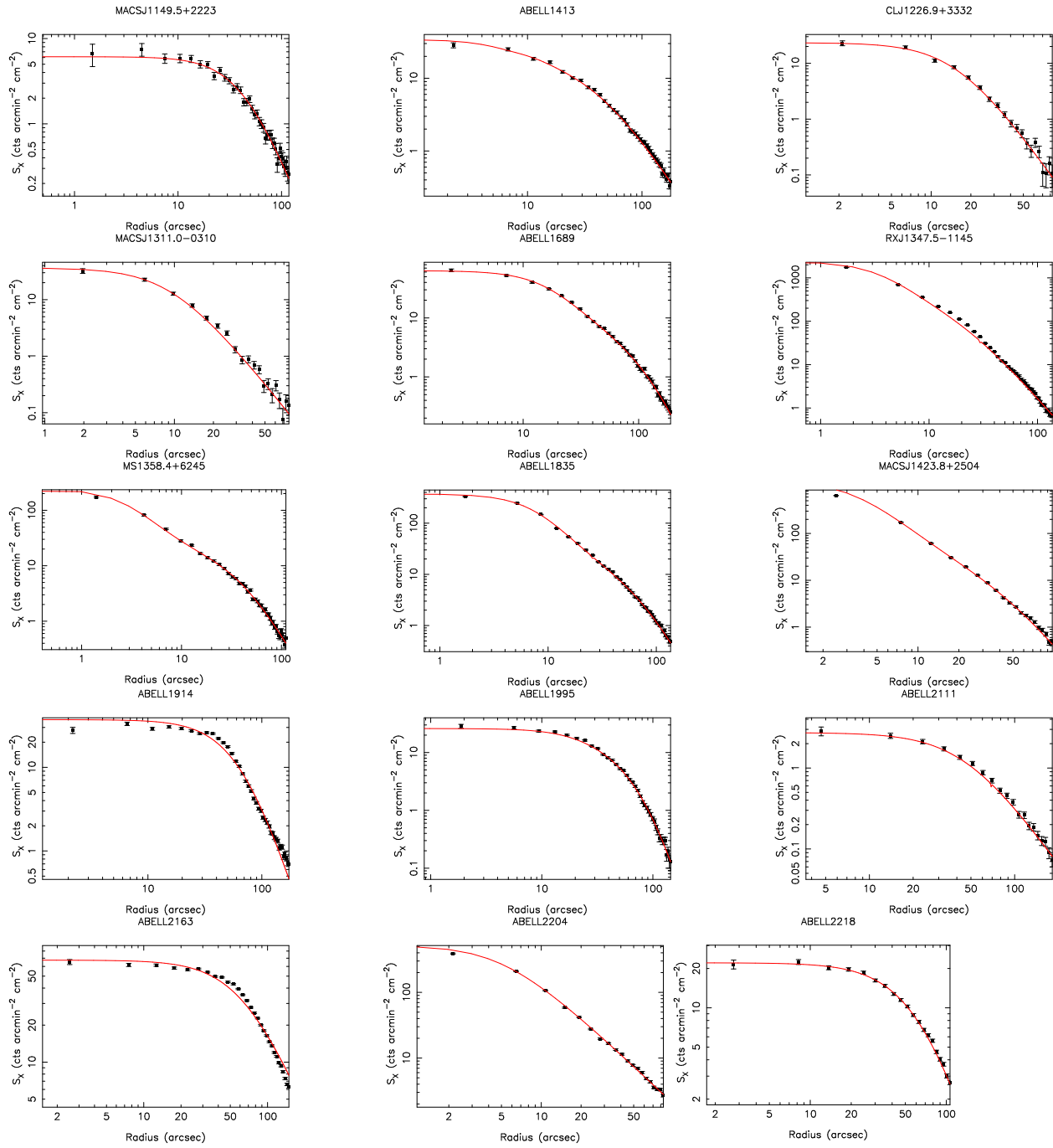


Appendix 2: Surface brightness profiles

In Figure 6 we show the radial profiles of the X-ray surface brightness for the 38 clusters in our sample. The χ^2 of the hydrostatic equilibrium model fits to the surface brightness profiles are shown in Table 2.

Fig. 6.— Background subtracted X-ray surface brightness profiles of the 38 clusters in our sample, with best-fit curves from the hydrostatic model results.





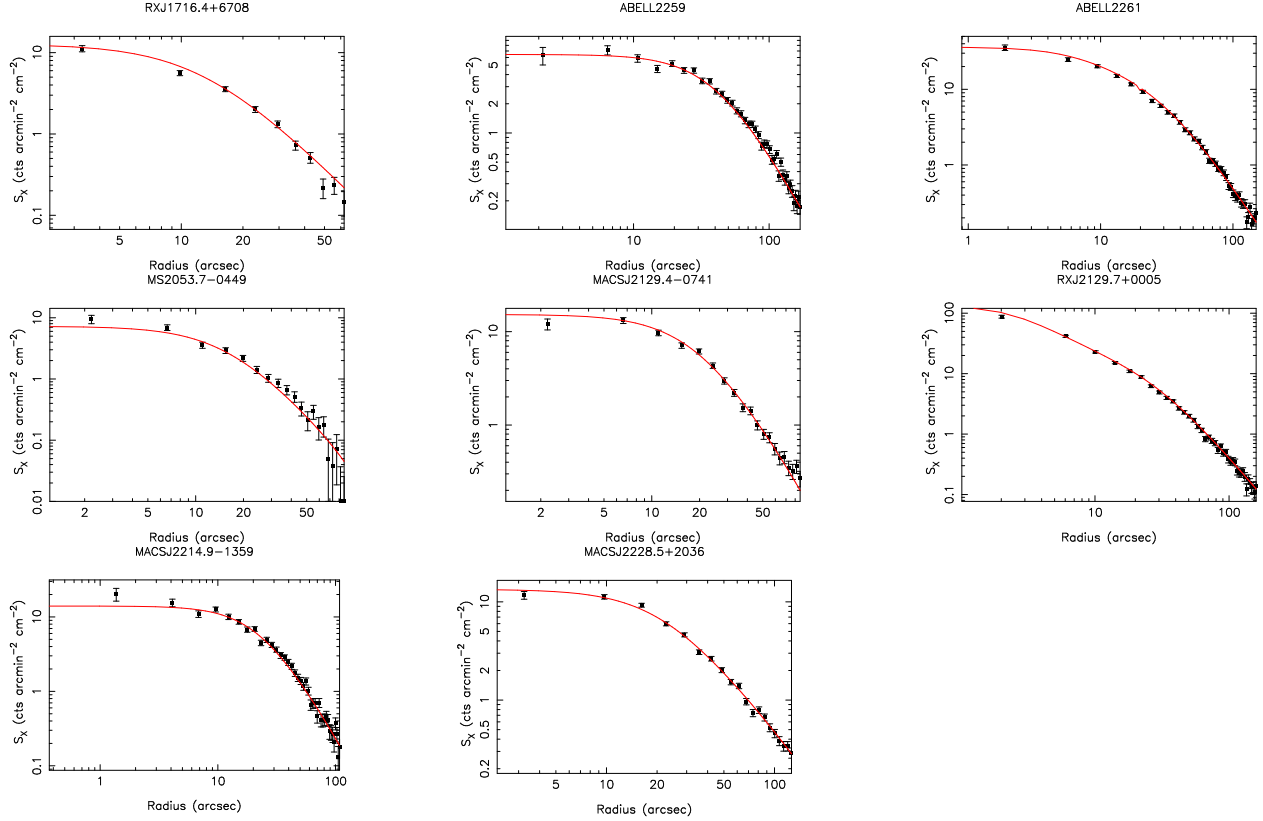


Table 6. Reduced χ^2 values of the hydrostatic equilibrium model fits to X-ray surface brightness profiles

Cluster	χ^2_r	Cluster	χ^2_r	Cluster	χ^2_r	Cluster	χ^2_r
CL0016+1609	1.38	Abell 697	1.12	RX J1347.5-1145	18.24	RX J1716.4+6708	0.97
Abell 68	0.90	Abell 773	0.98	MS 1358.4+6245	2.52	Abell 2259	1.47
Abell 267	0.74	ZW 3146	2.43	Abell 1835	3.31	Abell 2261	1.06
Abell 370	1.44	MS 1054-0321	1.40	MACS J1423+2404	17.60	MS 2053.7-0449	0.80
MS 0451.6-0305	1.28	MS 1137.5+6625	0.71	Abell 1914	15.29	MACS J1229.4-0741	1.24
MACS J0647.7+7015	1.07	MACS J1149.5+2223	1.14	Abell 1995	1.23	RX J2129.7+0005	1.15
Abell 586	1.30	Abell 1413	1.47	Abell 2111	1.39	MACS J2214.9-1359	1.38
MACS J0744.8+3927	1.18	CL J1226.9+3332	1.34	Abell 2163	41.62	MACS J2228.5+2036	1.11
Abell 611	1.40	MACS J1311.0-0310	1.47	Abell 2204	3.04		
Abell 665	11.84	Abell 1689	1.25	Abell 2218	1.22		

Appendix 3: Temperature profiles

Table 7. Temperature profiles

r (arcsec)	Counts	kT (keV)	χ^2 (dof)
CL 0016+1609 – Obs. 520			
0-17	2198.3	10.2 ± 2.2	73.5 (68)
17-24	1773.6	9.3 ± 2.2	64.1 (58)
24-32	1671.8	9.8 ± 2.3	68.7 (54)
32-42	2224.6	10.1 ± 2.7	86.4 (71)
42-52	2070.9	8.8 ± 1.7	84.9 (66)
52-65	1946.2	9.1 ± 2.0	64.6 (67)
65-83	1934.0	11.1 ± 3.0	64.6 (70)
83-101	1355.0	10.1 ± 3.1	39.6 (58)
Abell 0068 – Obs. 3250			
0-49	2036.9	10.8 ± 2.8	70.5 (67)
49-111	1910.0	7.5 ± 1.8	67.0 (65)
Abell 0267 – Obs. 1448			
0-53	1998.4	6.0 ± 0.9	71.1 (60)
53-166	1658.0	5.5 ± 1.2	50.6 (65)
Abell 0370 – Obs. 515			
0-13	1071.9	9.1 ± 3.1	23.4 (37)
13-21	1434.9	13.3 ± 5.2	38.6 (47)
21-28	1654.3	8.5 ± 2.0	67.8 (55)
28-36	1842.9	9.1 ± 2.3	59.4 (59)
36-40	965.5	8.6 ± 2.6	33.6 (34)
40-47	1876.2	13.1 ± 4.5	75.3 (63)
47-55	1718.9	10.1 ± 3.2	72.1 (60)
55-62	1591.6	7.1 ± 1.7	41.3 (57)
62-70	1381.4	8.5 ± 2.7	58.0 (53)
70-81	1856.6	7.3 ± 1.9	63.2 (76)
81-89	1004.7	6.1 ± 2.3	62.3 (46)
89-107	1942.2	6.8 ± 1.7	76.0 (93)

Table 7—Continued

r (arcsec)	Counts	kT (keV)	χ^2 (dof)
107-134	1880.2	5.4 ± 1.5	129.8 (116)
MS 0451.6-0305 – Obs. 529			
0-44	2002.3	7.9 ± 1.5	63.3 (62)
44-119	1317.6	6.8 ± 2.0	51.2 (57)
MS 0451.6-0305 – Obs. 902			
0-14	1922.4	14.3 ± 4.6	41.2 (59)
14-23	2226.5	9.3 ± 1.9	77.5 (67)
23-29	1476.1	8.3 ± 1.8	34.1 (49)
29-38	1985.2	9.6 ± 2.0	73.7 (64)
38-50	2171.4	10.3 ± 2.4	72.8 (71)
50-68	2123.6	9.1 ± 2.2	60.7 (73)
68-101	2008.7	10.8 ± 4.7	116.3 (87)
MACS J0647.7+7015 – Obs. 3196			
0-37	1973.8	12.4 ± 3.1	56.6 (65)
37-128	1323.0	10.5 ± 4.5	66.3 (65)
MACS J0647.7+7015 – Obs. 3584			
0-34	1885.6	10.7 ± 2.4	57.3 (60)
34-160	1790.8	19.1 ± 10.8	64.2 (83)
Abell 0586 – Obs. 530			
0-24	1909.4	7.8 ± 1.5	47.2 (60)
24-43	1925.4	7.7 ± 1.6	75.2 (62)
43-70	1939.5	6.9 ± 1.2	58.8 (63)
70-130	2062.0	6.4 ± 1.2	74.3 (73)
MACS J0744.8+3927 – Obs. 3197			
0-36	1948.1	8.47 ± 1.42	64.6 (62)

Table 7—Continued

r (arcsec)	Counts	kT (keV)	χ^2 (dof)
36-125	1108.9	9.15 ± 4.76	59.8 (57)
MACS J0744.8+3927 – Obs. 3585			
0-41	2019.9	8.1 ± 1.3	96.2 (65)
41-60	359.2	6.0 ± 2.3	18.2 (13)
Abell 0611 – Obs. 3194			
0-11	1916.2	6.0 ± 0.8	73.9 (60)
11-19	1268.4	7.3 ± 1.3	87.1 (79)
19-24	1351.4	6.0 ± 1.2	44.3 (44)
24-32	2341.6	6.7 ± 1.3	96.8 (74)
32-41	1850.1	6.0 ± 1.1	67.8 (57)
41-49	1487.9	7.1 ± 1.4	52.6 (51)
49-66	2279.9	5.9 ± 1.0	91.4 (78)
66-88	1857.0	6.0 ± 1.1	49.1 (71)
88-126	1982.7	6.8 ± 2.1	121.5 (102)
Abell 0665 – Obs. 3586			
0-19	2240.2	7.8 ± 1.4	72.3 (69)
19-26	1442.0	9.2 ± 2.7	42.1 (49)
26-37	2277.0	8.5 ± 1.7	94.1 (70)
37-47	2140.0	7.8 ± 1.4	68.2 (67)
47-58	2085.3	7.7 ± 1.5	53.3 (66)
58-69	1958.1	9.0 ± 2.3	80.0 (64)
69-79	1950.6	9.2 ± 2.3	66.5 (66)
79-90	1838.9	7.4 ± 1.7	44.5 (61)
90-100	1825.5	7.3 ± 1.6	48.7 (61)
100-111	1727.1	9.7 ± 2.9	63.4 (59)
111-125	2149.2	8.3 ± 1.8	88.8 (74)
125-139	1989.6	8.7 ± 2.2	78.0 (68)

Table 7—Continued

r (arcsec)	Counts	kT (keV)	χ^2 (dof)
Abell 0665 – Obs. 531			
0-37	2029.8	6.7 ± 1.1	58.7 (62)
37-67	1904.4	8.8 ± 2.2	60.3 (60)
67-103	2006.3	11.9 ± 3.6	65.8 (66)
Abell 0697 – Obs. 4217			
0-25	2176.0	10.1 ± 2.3	67.7 (67)
25-39	2031.6	10.2 ± 2.6	76.6 (63)
39-48	1397.5	9.1 ± 2.6	44.3 (46)
48-67	2213.1	11.2 ± 2.9	74.1 (70)
67-90	2117.5	10.8 ± 2.8	61.4 (70)
90-117	2029.7	12.6 ± 4.0	66.6 (73)
117-154	1914.1	9.9 ± 2.8	81.8 (72)
Abell 0773 – Obs. 3588			
0-41	1930.5	6.0 ± 1.0	75.2 (61)
41-80	1934.3	6.2 ± 1.2	89.4 (63)
80-157	2066.8	6.4 ± 1.3	72.3 (73)
Abell 0773 – Obs. 533			
0-36	1990.2	7.2 ± 1.4	66.9 (61)
36-62	1900.2	8.6 ± 2.1	61.3 (61)
62-106	2019.5	7.1 ± 1.3	67.0 (67)
ZW 3146 – Obs. 909			
0-5	3491.4	3.9 ± 0.2	133 .6 (130)
5-11	7557.8	4.9 ± 0.2	213.8 (154)
11-18	8887.2	6.5 ± 0.3	218.0 (176)
18-25	6361.8	7.0 ± 0.3	180.7 (150)
25-35	6237.6	8.4 ± 0.6	158.3 (150)
35-46	5598.2	8.2 ± 0.6	109.3 (140)

Table 7—Continued

r (arcsec)	Counts	kT (keV)	χ^2 (dof)
46-60	4756.4	9.1 ± 0.6	153.1 (134)
60-76	3401.7	9.7 ± 1.2	83.5 (109)
76-101	3252.7	8.7 ± 0.9	91.8 (115)
101-140	2238.8	7.7 ± 1.2	101.7 (89)
MS 1054-0321 – Obs. 512			
0-14	740.3	13.8 ± 6.3	27.7 (26)
14-22	937.0	7.7 ± 2.6	26.1 (33)
22-35	1755.5	9.6 ± 2.1	66.7 (62)
35-50	1718.1	13.2 ± 4.7	65.1 (68)
50-83	1751.9	8.7 ± 3.5	131.7 (109)
MS 1137.5+6625 – Obs. 536			
0-25	1585.5	6.4 ± 1.2	56.1 (52)
25-75	897.7	4.6 ± 1.4	43.5 (55)
MACS J1149.5+2223 – Obs. 1656			
0-48	1924.1	9.30 ± 1.97	68.3 (63)
48-108	1702.6	7.71 ± 1.90	50.4 (65)
MACS J1149.5+2223 – Obs. 3589			
0-46	1985.5	10.8 ± 2.5	64.67 (66)
46-112	1911.5	7.0 ± 1.6	57.6 (71)
Abell 1413 – Obs. 1661			
0-20	2190.8	6.0 ± 0.9	68.1 (67)
20-34	2040.8	9.0 ± 2.0	63.6 (64)
34-47	2005.8	8.3 ± 1.5	57.0 (64)
47-61	1640.5	9.2 ± 2.4	55.7 (54)
61-79	1841.1	7.4 ± 1.6	57.5 (60)
79-106	2156.7	6.0 ± 1.0	78.4 (68)

Table 7—Continued

r (arcsec)	Counts	kT (keV)	χ^2 (dof)
106-133	1789.5	6.2 ± 1.0	61.7 (59)
133-178	1982.4	7.4 ± 1.7	76.6 (74)
Abell 1413 – Obs. 537			
0-18	1908.9	7.1 ± 1.5	55.5 (59)
18-31	1973.0	8.2 ± 1.8	62.3 (62)
31-46	2129.7	6.2 ± 1.0	79.1 (63)
46-62	1823.0	7.0 ± 1.3	49.6 (58)
62-81	2045.6	9.2 ± 2.3	85.3 (65)
CL J1226.9+3332 – Obs. 3180			
0-82	1962.2	12.1 ± 2.6	58.8 (63)
CL J1226.9+3332 – Obs. 932			
0-58	1003.9	15.4 ± 7.5	26.9 (35)
MACS J1311.0-0310 – Obs. 3258			
0-73	1963.2	6.7 ± 1.1	76.3 (65)
Abell 1689 – Obs. 1663			
0-12	2136.8	9.4 ± 2.1	76.3 (67)
12-17	1409.5	9.5 ± 2.9	47.0 (45)
17-26	2928.5	9.47 ± 1.81	94.7 (87)
26-31	1271.1	16.57 ± 9.01	41.0 (42)
31-41	2159.3	9.41 ± 2.09	65.9 (67)
41-50	1922.3	9.77 ± 2.69	72.0 (63)
50-60	1687.4	8.72 ± 2.18	59.7 (54)
60-74	2150.8	9.78 ± 2.28	75.1 (68)
74-93	2244.1	14.10 ± 4.95	81.6 (72)
93-117	2012.4	9.22 ± 2.14	59.6 (68)
117-146	1759.2	10.55 ± 3.27	56.7 (61)
146-189	1532.9	6.53 ± 1.57	51.2 (59)

Table 7—Continued

r (arcsec)	Counts	kT (keV)	χ^2 (dof)
Abell 1689 – Obs. 540			
0-10	1601.5	11.9 ± 3.8	64.8 (51)
10-18	2431.2	7.8 ± 1.3	97.7 (71)
18-24	1706.8	8.0 ± 1.6	47.5 (53)
24-32	2236.1	13.1 ± 3.8	59.1 (68)
32-41	1798.6	13.4 ± 5.0	57.5 (59)
41-52	2178.3	9.7 ± 2.1	82.2 (68)
52-63	1890.4	11.0 ± 3.0	66.6 (60)
63-78	2035.9	14.7 ± 5.2	59.5 (67)
78-94	1898.7	11.7 ± 4.9	61.4 (60)
94-111	1371.4	12.7 ± 4.7	53.0 (46)
RX J1347.5-1145 – Obs. 3592			
0-2	2062.7	6.3 ± 0.9	95.9 (103)
2-5	7479.7	8.5 ± 0.7	208.3 (166)
5-9	6539.0	11.2 ± 1.3	192.2 (159)
9-12	5672.1	16.3 ± 3.1	199.6 (151)
12-16	4939.2	14.8 ± 2.9	166.5 (137)
16-19	4392.6	16.8 ± 3.4	159.7 (126)
19-23	4010.0	14.6 ± 3.0	106.2 (122)
23-29	5869.5	13.5 ± 2.0	182.8 (154)
29-36	4081.0	18.4 ± 4.2	115.7 (124)
36-47	4143.3	19.1 ± 4.3	158.9 (128)
47-68	5440.7	14.1 ± 2.5	171.7 (154)
68-102	4970.9	12.8 ± 2.5	161.3 (154)
MS 1358.4+6245 – Obs. 516			
0-7	2112.3	4.02 ± 0.38	61.4 (63)
7-13	1629.5	5.92 ± 1.18	39.3 (50)
13-21	2237.5	8.36 ± 1.71	65.9 (71)

Table 7—Continued

r (arcsec)	Counts	kT (keV)	χ^2 (dof)
21-29	2038.2	8.8 ± 1.8	63.4 (66)
29-41	2143.1	9.2 ± 2.2	96.1 (68)
41-52	1928.4	8.6 ± 2.1	66.2 (66)
52-66	1726.7	7.5 ± 2.0	50.0 (62)
66-88	1959.2	8.1 ± 2.3	94.3 (82)
88-111	1203.9	12.6 ± 9.9	46.7 (67)
Abell 1835 – Obs. 495			
0-5	4283.1	4.3 ± 0.4	121.3 (101)
5-9	4989.8	5.0 ± 0.4	117.7 (114)
9-12	4033.2	6.3 ± 0.7	117.6 (104)
12-19	6163.1	9.1 ± 1.1	142.9 (140)
19-26	4943.0	8.3 ± 1.1	143.5 (121)
26-36	5573.5	9.1 ± 1.2	150.2 (133)
36-46	4466.6	12.6 ± 2.4	146.1 (125)
46-64	5255.3	9.2 ± 1.3	116.4 (129)
64-91	5233.8	11.6 ± 2.2	162.7 (142)
901-136	4718.5	18.4 ± 7.2	135.3 (151)
Abell 1835 – Obs. 496			
0-11	5201.4	5.0 ± 0.4	95.6 (117)
11-20	3868.4	7.0 ± 0.9	111.6 (103)
20-42	6416.7	8.2 ± 0.9	173.9 (142)
42-68	4488.9	11.2 ± 2.5	110.7 (120)
68-138	4982.1	13.4 ± 4.0	139.0 (143)
MACS J1423.8+2404 – Obs. 4195			
0-3	2988.9	4.2 ± 0.4	97.4 (87)
3-8	7992.4	4.8 ± 0.3	199.7 (146)
8-13	4588.5	6.6 ± 0.6	106.6 (118)
13-18	2869.9	7.4 ± 1.0	66.1 (87)

Table 7—Continued

r (arcsec)	Counts	kT (keV)	χ^2 (dof)
18-23	2169.4	7.4 ± 1.2	72.9 (66)
23-28	1731.4	7.2 ± 1.5	47.6 (54)
28-32	1459.8	8.7 ± 2.2	52.8 (49)
32-38	1140.1	6.1 ± 1.4	44.2 (41)
38-42	943.7	7.0 ± 2.2	28.9 (37)
42-47	739.6	6.9 ± 3.3	34.1 (29)
47-52	657.5	5.9 ± 2.1	19.5 (28)
52-57	553.7	7.4 ± 3.9	15.9 (25)
57-62	484.9	6.8 ± 4.2	14.5 (24)
62-67	477.5	7.0 ± 6.5	34.0 (24)
67-77	806.5	5.4 ± 2.0	38.3 (47)
77-97	1075.9	4.6 ± 1.4	73.0 (77)
Abell 1914 – Obs. 3593			
0-24	4677.0	13.1 ± 2.5	125.6 (138)
24-37	5716.9	11.3 ± 1.7	184.5 (154)
37-46	4416.5	11.0 ± 1.9	117.5 (130)
46-55	4180.6	11.4 ± 2.3	117.6 (126)
55-72	6022.7	8.5 ± 1.1	150.1 (152)
72-94	4535.4	11.5 ± 2.3	167.2 (132)
94-138	5294.2	8.9 ± 1.3	144.8 (154)
138-173	2636.7	8.2 ± 1.8	100.7 (93)
Abell 1914 – Obs. 542			
0-25	2276.3	10.8 ± 2.7	62.5 (69)
25-32	1345.1	13.4 ± 6.7	43.2 (44)
32-44	2278.0	10.8 ± 2.8	55.7 (69)
44-51	1613.1	16.7 ± 6.8	47.9 (53)
51-63	2160.2	13.6 ± 4.1	71.4 (66)
63-78	2050.4	10.9 ± 3.2	65.2 (64)
78-104	2186.0	8.8 ± 2.2	71.7 (69)

Table 7—Continued

r (arcsec)	Counts	kT (keV)	χ^2 (dof)
104-142	1849.5	8.4 ± 2.4	61.2 (66)
Abell 1995 – Obs. 906			
0-13	2060.1	7.8 ± 1.4	51.9 (64)
13-17	1120.6	10.2 ± 4.0	38.3 (37)
17-24	2658.1	7.4 ± 1.3	72.9 (78)
24-28	1461.6	9.3 ± 2.8	45.5 (47)
28-36	2715.0	9.9 ± 2.0	60.4 (84)
36-39	1293.1	13.0 ± 4.9	34.5 (43)
39-47	2449.4	9.1 ± 2.2	98.2 (75)
47-54	2228.6	10.0 ± 2.7	86.8 (73)
54-62	1814.6	7.1 ± 1.3	68.4 (61)
62-69	1557.0	7.2 ± 1.6	55.2 (55)
69-84	2209.6	8.2 ± 2.0	83.9 (85)
84-107	1992.8	11.1 ± 4.6	92.1 (92)
107-148	1805.4	8.4 ± 4.7	149.8 (131)
Abell 2111 – Obs. 544			
0-70	2114.6	7.5 ± 1.50	75.2 (66)
70-163	1932.3	9.3 ± 3.0	87.6 (70)
Abell 2163 – Obs. 1653			
0-23	8821.2	18.07 ± 4.57	210.6 (201)
23-33	9098.7	11.62 ± 2.20	243.6 (199)
33-43	11446.3	19.36 ± 4.33	256.4 (228)
43-53	12904.6	12.71 ± 1.89	260.6 (243)
53-58	6900.5	11.4 ± 2.3	173.0 (174)
58-68	13317.5	13.6 ± 1.9	231.4 (246)
68-73	6111.6	11.7 ± 2.1	177.8 (164)
73-83	11752.2	15.0 ± 2.8	249.0 (235)
83-93	10457.4	13.1 ± 2.2	231.6 (221)

Table 7—Continued

r (arcsec)	Counts	kT (keV)	χ^2 (dof)
93-103	9532.6	16.3 ± 3.7	213.3 (212)
103-113	8423.0	16.5 ± 4.0	205.4 (202)
113-129	10962.5	18.5 ± 4.5	257.2 (233)
129-144	8863.9	14.6 ± 3.1	191.3 (207)
144-164	10300.9	17.1 ± 4.7	231.2 (231)
164-184	9774.5	14.5 ± 3.0	275.3 (232)
184-199	6843.6	18.1 ± 6.1	173.2 (195)
Abell 2204 – Obs. 499			
0-7	4961.3	3.6 ± 0.2	105.5 (114)
7-11	4238.5	4.3 ± 0.3	115.8 (108)
11-19	5979.5	5.7 ± 0.5	166.5 (136)
19-28	3962.0	8.1 ± 1.2	110.2 (111)
28-45	6013.9	9.4 ± 1.3	145.1 (144)
45-62	4447.9	9.4 ± 1.6	118.5 (122)
62-93	5059.2	10.8 ± 2.0	104.3 (137)
93-153	5317.6	13.4 ± 4.0	148.0 (151)
Abell 2204 – Obs. 6104			
0-6	3805.5	3.3 ± 0.2	125.1 (105)
6-15	5643.9	5.4 ± 0.4	196.7 (142)
15-28	5274.9	7.3 ± 0.8	192.0 (138)
28-45	4774.2	11.1 ± 1.9	130.7 (136)
45-75	5517.0	9.3 ± 1.2	142.9 (151)
Abell 2218 – Obs. 1666			
0-30	5103.0	9.2 ± 1.2	135.4 (142)
30-46	4969.6	8.9 ± 1.3	128.5 (141)
46-63	4936.2	8.0 ± 1.1	145.5 (140)
63-79	4515.1	8.3 ± 1.2	144.7 (136)
79-107	5582.4	6.5 ± 0.7	151.1 (153)

Table 7—Continued

r (arcsec)	Counts	kT (keV)	χ^2 (dof)
RX J1716.4+6708 – Obs. 584			
0-62	1428.3	7.1 ± 1.6	54.2 (57)
Abell 2259 – Obs. 3245			
0-41	1933.3	5.3 ± 0.7	82.4 (62)
41-79	2113.1	5.0 ± 0.7	67.0 (65)
79-135	1830.5	5.4 ± 0.9	83.3 (63)
Abell 2261 – Obs. 550			
0-17	1801.4	6.8 ± 1.4	73.1 (57)
17-36	2244.5	7.4 ± 1.4	94.4 (67)
36-59	1874.8	7.0 ± 1.5	50.0 (59)
59-100	1957.3	9.3 ± 2.2	66.9 (67)
100-150	1140.8	5.8 ± 1.6	38.2 (47)
MS 2053.7-0449 – Obs. 1667			
0-86	1095.1	3.8 ± 0.9	36.0 (57)
MS 2053.7-0449 – Obs. 551			
0-117	1188.4	6.7 ± 2.8	87.4 (79)
MACS J2129.4-0741 – Obs. 3199			
0-46	2012.3	7.1 ± 1.1	63.4 (66)
46-90	651.2	5.5 ± 1.7	38.7 (30)
MACS J2129.4-0741 – Obs. 3595			
0-42	1974.1	12.3 ± 2.9	55.6 (65)
42-90	875.8	8.7 ± 3.7	41.2 (37)
RX J2129.7+0005 – Obs. 552			
0-14	1852.5	4.4 ± 0.5	57.2 (57)

Table 7—Continued

r (arcsec)	Counts	kT (keV)	χ^2 (dof)
14-34	2160.4	6.1 ± 0.9	65.9 (65)
34-67	1931.2	6.4 ± 1.0	75.4 (64)
67-159	1970.1	7.4 ± 1.6	85.2 (73)
MACS J2214.9-1359 – Obs. 3259			
0-32	1882.6	9.5 ± 2.4	64.2 (60)
32-95	2099.3	15.1 ± 5.0	82.1 (76)
MACS J2214.9-1359 – Obs. 5011			
0-40	2030.9	10.6 ± 2.8	75.4 (64)
40-119	1691.7	8.6 ± 2.6	50.0 (67)
MACS J2228.5+2036 – Obs. 3285			
0-29	1835.3	8.4 ± 1.7	58.5 (59)
29-68	2140.5	8.9 ± 1.9	53.3 (68)
68-126	1605.8	10.5 ± 3.6	57.8 (67)